Particle dynamics predicts shear rheology of soft particle glasses

Fardin Khabaz, Michel Cloitre, Roger Bonnecaze

Particle Dynamics Predicts Shear Rheology of Soft Particle Glasses

Fardin Khabaz,[1] Michel Cloitre,[2] and Roger T. Bonnecaze[1*]

[1]McKetta Department of Chemical Engineering, The University of Texas at Austin,

Austin, TX, 78712, USA

[2]Molecular, Macromolecular Chemistry, and Materials, ESPCI Paris, CNRS, PSL University,

10 Rue Vauquelin, 75005 Paris, France

[*]Corresponding author e-mail: rtb@che.utexas.edu

Abstract

Soft particle glasses are amorphous materials made of soft and deformable particles that are jammed above close-packing. They behave like weak solids at rest but they yield and flow under external mechanical constraints. Although soft particle glasses are widely used in applications, little is known about how the particle softness and microscopic dynamics determine the macroscopic rheology. Here we use three-dimensional particle dynamic simulations to analyze the dynamical properties of soft particle glasses at different scales. We demonstrate how the dynamics is determined by the persistence time and the magnitude of the fluctuating elastic forces that develop at contact in the flow. The shear-induced diffusion coefficient, the local structural relaxation times, the shear stress, and the normal stress differences are interconnected through simple relationships that allow the prediction of the macroscopic rheology from the microscopic dynamics.

I. INTRODUCTION

Soft particle glasses (SPGs) are amorphous materials composed of deformable particles jammed at volume fractions beyond close-packing where they are in contact and interact through elastic forces [1, 2]. They include many systems of practical interest such as concentrated emulsions, microgel pastes, micelles, or star polymer solutions. In SPGs each particle is constrained in a cage by elastic forces and cannot move over long distances unless an external stress larger than the yield stress σ_y is applied. The flow curve that relates the shear stress σ to the shear rate $\dot{\gamma}$ is well described by the generic Herschel-Bulkley equation $\sigma = \sigma_y + k\dot{\gamma}^n$ [3, 4]; the first and second normal stress differences follow similar relations [4]. An open and important question concerns the physical origin of these empirical equations and their connection with the particle scale dynamics of SPGs.

Recent experiments have established that the microscopic dynamics of glasses and jammed materials is characterized by shear-induced structural rearrangements that generate stress and strain fluctuations propagating via elastic interactions [5-12]. Theoretical investigations, which are mainly based on 2D simulations and numerical models, have shown that long-range plastic relaxation modes are associated with dynamical heterogeneities consisting of spatiotemporal patterns where particle displacements are correlated [13-20]. The geometry of the heterogeneities depend on the flow rate [12] and their size diverges at low shear rates making low-shear properties system-size dependent. Shear induced rearrangements are responsible for self-diffusion whose properties has been connected to the characteristic of cooperative regions at low strain rates [6, 7, 14, 17, 18, 20]. An important consequence of the existence of spatiotemporal heterogeneities is that mean-field approximations do not accurately connect microscopic processes to rheology [21, 22].

Although this framework captures important features of the microscopic dynamics of glassy materials, it poses several important questions. First, most existing results are strictly valid for 2D systems and 3D investigations are clearly needed. Secondly, little attention has been paid to the very nature of the interaction potential. SPGs are singular in this context since particles interact through elastic potential that are much softer than hard sphere or Lennard Jones potentials often used in previous investigations. Elastic deformations caused by soft potentials have been shown to play an important role in the dynamics of soft colloids [4, 23, 24]. In brief the connection between non affine particle trajectories, mesoscopic properties and macroscopic rheology in real 3D SPGs remains an outstanding challenge.

Here we address this question using three-dimensional particle simulations of non-Brownian deformable particles in the jamming regime where elastic contact forces are dominant [4]. We show that at short time, the sustained elastic forces exerted by the particles at contact are responsible for ballistic motion whereas at long time the non-affine dynamics are diffusive with a shear-dependent diffusion coefficient. We characterize the single particle dynamics using the elastic force autocorrelation function and the intermediate scattering function that provides microscopic relaxation rates. The shear-induced diffusion coefficient, the microstructural relaxation time, shear stress, and normal stress differences are controlled by the persistence time of the local elastic forces which also sets the duration of the short time ballistic motion. They are found to be universal functions of a non-dimensional shear rate $\hat{\dot{\gamma}} = \dot{\gamma}\eta_s / G_0$ that characterizes the competition between the advection time $\dot{\gamma}^{-1}$ and the cage relaxation time η_s / G_0 (η_s is the solvent viscosity and G_0 is the cage elasticity [25]). The macroscopic rheology and the local relaxation rate can be deduced one from the other, suggesting a method to extract the global rheology of SPGs from microrheological data.

II. Model and Simulations

The details of the model and the simulation method have been presented in previous studies [4, 26-29]. Below we briefly summarize the important features. Soft particle glasses are modeled as suspensions of N non-Brownian elastic particles in a solvent with a viscosity η_s, which are jammed in a cubic simulation box at volume fractions larger than the random close-packing of hard spheres (Fig. 1). $N = 1000$ in most of the simulations reported in this work and we checked that the results are not affected by finite size effects. Suspensions with an average radius of unity, polydispersity index of $\delta = 0.2$, and volume fractions of $\phi = 0.7, 0.75, 0.8, 0.85$, and 0.9 are studied. The value of the polydispersity agrees with that currently found in experiments [4, 29], and it prevents crystallization at high shear rates [27, 28]. Because the particles are compressed, they have a polyhedral shape with flat facets at contact instead of their initial spherical shape. We have shown that these elastic contacts are central to the rheological properties of SPGs [4, 25].

The initial preparation of the suspensions proceeds as follows. A glass-like structure is first created using the Lubachevsky and Stillinger algorithm [30, 31]. The close-packed configurations are compressed by reducing the box size in small steps until the desired volume fraction is achieved. The volume fraction of the suspension is computed as the ratio between the total volume of the particles and the volume of the box. After each compressive step, the system is allowed to relax using the conjugate gradient algorithm so that there is no net force on any of the particles. At contact, particles α and β create a flat facet resulting in a deformation of $\varepsilon_{\alpha,\beta} = 0.5\left(R_\alpha + R_\beta - r_{\alpha\beta}\right)\big/R_c$, where R_α and R_β are the radii of particle α and β, $r_{\alpha\beta}$ is the center-to-center distance, and R_c is the contact radius, which is given as $R_c = R_\alpha R_\beta \big/ \left(R_\alpha + R_\beta\right)$. $\mathbf{n}_\perp$ and

$\mathbf{n}_{\|}$ are unit vectors along the perpendicular and parallel directions to the facet, respectively (Fig. 1).

The elastic repulsion force between particles α and β acts perpendicularly to the contacting facet. It is given by the generalized Hertz law [4]:

$$\mathbf{f}_{\alpha\beta}^{e} = \frac{4}{3} C E^{*} \varepsilon_{\alpha\beta}^{n} R_{c}^{2} \mathbf{n}_{\perp}, \tag{1}$$

where E^{*} is the particle contact modulus: $E^{*} = E/2\left(1-\nu^{2}\right)$, with E being the Young modulus and ν is the Poisson ratio. The Poisson ratio is taken equal to 0.5 in these simulations so that the volume of the particle upon deformation remains constant. Moreover the particles are not allowed to deswell by osmotic effect when the volume fraction increases contrary to what has been reported in microgels [32, 33]. C and n are parameters, which depend on the degree of compression. For $\varepsilon < 0.1$ $n = 1.5$ and $C = 1$, for $0.1 \le \varepsilon < 0.2$ $n = 3$ and $C = 32$, and if $0.2 \le \varepsilon < 0.6$ $n = 5$ and $C = 790$ [4, 34]. The elastohydrodynamic (EHD) drag force, which is due to the existence of thin films of solvent between the flat facets of two particles in contact during the shear deformation [4], is parallel to the contacting facets and is given by:

$$\mathbf{f}_{\alpha\beta}^{\mathrm{EHD}} = -\left(\eta_{s} C u_{\alpha\beta,\|} E^{*} R_{c}^{3}\right)^{1/2} \varepsilon_{\alpha\beta}^{(2n+1)/4} \mathbf{n}_{\|}, \tag{2}$$

where $u_{\alpha\beta,\|}$ is the relative velocity component in the direction of $\mathbf{n}_{\|}$. The fluid inertia is neglected and the forces are assumed to be pair-wise additive. The velocity field due to the motion of the solvent is given as $\mathbf{u}_{\alpha}^{\infty} = \frac{\dot{\gamma}\eta_{s}}{E^{*}} y \mathbf{e}_{x}$, where $\mathbf{e}_{\mathrm{x}}$ is the basis vector in the x-direction. The resulting equation of motion is made dimensionless by scaling lengths, time and velocity by R, $\dot{\gamma}^{-1}$ and $\dot{\gamma}R$ respectively, leading to [4, 26, 29]:

$$\frac{d\tilde{\mathbf{x}}_\alpha}{dt} = \tilde{\mathbf{u}}_\alpha^\infty + \frac{M}{\tilde{R}_\alpha}\left[\frac{4}{3}C\tilde{\dot{\gamma}}^{-1}\sum_\beta \varepsilon_{\alpha\beta}^n \tilde{R}_c^2 \mathbf{n}_\perp - \tilde{\dot{\gamma}}^{-1/2}\sum_\beta \left(C\tilde{u}_{\alpha\beta,\parallel}\tilde{R}_c^3\right)^{1/2} \varepsilon_{\alpha\beta}^{(2n+1)/4}\mathbf{n}_\parallel\right], \quad (3)$$

where the tilde quantities are dimensionless variables. M is the mobility function which is that of a particle corrected by a factor $f(\phi)$ that accounts for its reduction at high volume fraction $(M = f(\phi)/6\pi)$; $f(\phi)$ is set to 0.01 in the simulations [35]. $\mathbf{x}_\alpha$ is the position of particle α. The form of this equation shows that the dynamics is characterized solely by the dimensionless shear rate $\tilde{\dot{\gamma}} = \dot{\gamma}\eta_s / E^*$, which represents the ratio of viscous to elastic forces, and the overlap deformation that depends on the volume fraction.

The Lees-Edwards [36] boundary conditions are then used in the LAMMPS package [37] in order to impart the desired shear rate to the simulation box. The stress tensor of the suspensions is determined using the Kirkwood formula [38]:

$$\boldsymbol{\sigma} = \frac{1}{V}\sum_\beta^N \sum_{\alpha>\beta}^N \mathbf{f}_{\alpha\beta}\left(\mathbf{x}_\alpha - \mathbf{x}_\beta\right), \quad (4)$$

where V is the volume of the system and $\mathbf{f}_{\alpha\beta}$ is the total force acting on particle α from particle β. The shear stress σ_{xy}, the first and second normal stress differences, $N_1 = \sigma_{xx} - \sigma_{yy}$ and $N_2 = \sigma_{yy} - \sigma_{zz}$, are computed from the appropriate components of the stress tensor. The flow properties of the suspensions are investigated over a broad range of shear rate ranging from $\tilde{\dot{\gamma}} = 10^{-9}$ to $\tilde{\dot{\gamma}} = 10^{-4}$. The simulations are performed for 100 strain units and the stress tensor is calculated at regular strain intervals. The value of the time step is chosen such that it produced 10^7 steps per strain at each shear rate.

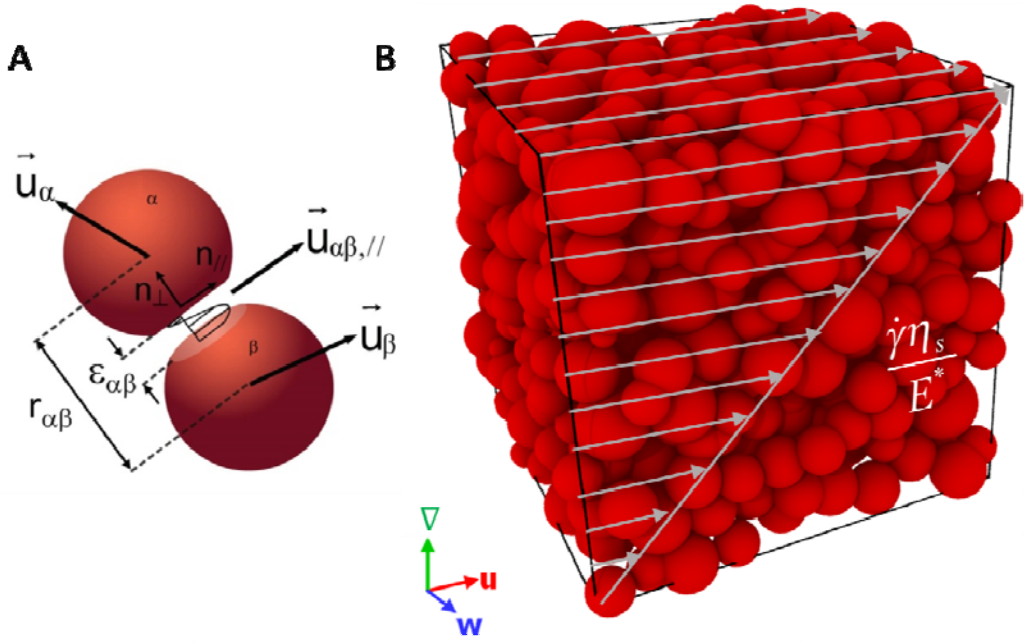

FIG. 1. (A) Schematic showing pair-wise interaction between particles α and β. (B) Configuration of a suspension with a volume fraction of 0.9 and polydispersity index of δ = 0.1 that is in shear flow. The flow (u), gradient (∇), and vorticity (w) directions are labeled on the axes.

III. Results

A. Macroscopic rheology

We have computed the linear and nonlinear dynamical properties of SPG for volume fractions of $\phi = 0.70, 0.75, 0.80, 0.85$, and 0.9. The low frequency shear modulus computed from the elastic forces that the particles exert on each other is shown in Table 1 [25]. At the particle scale level, G_0 also represents the so-called cage elasticity to which each particle is subjected as it is trapped by many neighbors [39].

TABLE I. Summary of rheological properties of SPGs used in this study

Volume fraction (ϕ)	Low frequency modulus (G_0/E^*)	Yield stress (σ_y/E^*)	Yield strain (γ_y)	HB exponent (n)
0.70	3.16×10^{-3}	8.4×10^{-5}	2.6×10^{-2}	0.49
0.75	7.02×10^{-3}	2.29×10^{-4}	3.2×10^{-2}	0.49
0.80	1.760×10^{-2}	5.49×10^{-4}	3.1×10^{-2}	0.46
0.85	3.638×10^{-2}	1.21×10^{-3}	3.3×10^{-2}	0.47
0.90	6.477×10^{-2}	2.38×10^{-3}	3.7×10^{-2}	0.47

We have also computed the shear stress (σ), first and second normal stress differences (N_1 and N_2) as a function of the dimensionless shear rate $\tilde{\dot{\gamma}} = \dot{\gamma}\eta_s / E^*$. The flow curves $\sigma(\tilde{\dot{\gamma}})$ and the normal stress differences $N_1(\tilde{\dot{\gamma}})$ and $N_2(\tilde{\dot{\gamma}})$ are shown in Fig. S1 with the raw data being reported in Table S1 in the Supplementary Materials. The first and second normal stress differences are of opposite signs and differ by only a factor 2 ($N_1(\tilde{\dot{\gamma}}) > 0$, $N_2(\tilde{\dot{\gamma}}) < 0$). It has been predicted that negative second normal stress difference of comparable magnitude to the first normal stress difference is a property of fluids which internal deformable interfaces such as emulsions, foams, and polymer blends which are called film fluids, [40]. They are well described by Herschel-Bulkley equations, whose parameters depend on the volume fraction as shown in Table 1. We have checked that the data are independent of the system size; simulations with 10^3, 10^4, and 1.25×10^5 particles lead to the same results (see Fig. S2). In particular the value and the extent of the low-shear stress plateau is not affected by finite size effects contrary to what has been reported in 2D simulations [15, 17, 20]. Following [1, 26, 41], in Fig. 2A the

shear stresses obtained for different volume fractions collapse onto a single Herschel-Bulkley master curve when they are scaled by the yield stress σ_y and plotted as a function of the dimensionless shear rate $\hat{\dot{\gamma}} = \dot{\gamma}\eta_s / G_0$. η_s is the solvent viscosity and G_0 is the static elastic modulus of the suspensions or the cage elasticity, which ultimately depends on the particle elasticity and volume fraction. When particles interact through the Hertz potential [1], the dimensionless variable $\hat{\dot{\gamma}}$ is equivalent to the form $\eta_s \dot{\gamma} / \gamma_y^2 E^*$ (γ_y is the yield strain) that was introduced in previous publications [4, 33]. The value of the Herschel-Bulkley exponent is $n \cong 0.48$. We emphasize that this scaling is valid only in the jammed glass regime where elastic contact forces are dominant; thermal glasses controlled by Brownian forces have a different behavior [33, 42]. In Fig. 2B, the first and second normal stress differences also collapse onto generic master curves against $\hat{\dot{\gamma}} = \dot{\gamma}\eta_s / G_0$ once they are normalized by the yield stress values σ_y. The non-dimensional shear rate $\hat{\dot{\gamma}}$ expresses the competition between the viscous forces and the elastic forces experienced by the jammed particles when they yield [41]. From the results shown in Fig. 2A-B, we anticipate the existence of two asymptotic regimes separated by a broad crossover around $\hat{\dot{\gamma}}_0 \cong 5 \times 10^{-6}$: a constant stress plateau at low shear rates $(\hat{\dot{\gamma}} < \hat{\dot{\gamma}}_0)$ and a power-law regime at high shear rates $(\hat{\dot{\gamma}} > \hat{\dot{\gamma}}_0)$. In the following we connect these macroscopic rheological properties to the local dynamics of SPGs.

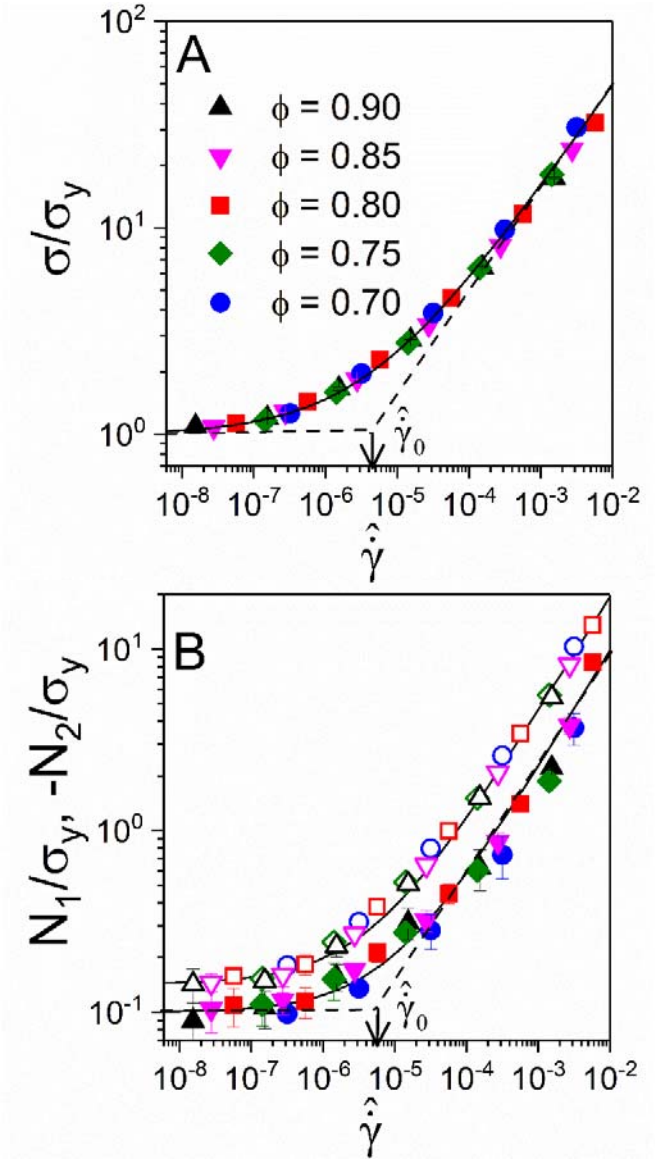

FIG. 2. Macroscopic flow properties of SPGs. (A) Shear stress σ and (B) first (closed symbols) and second (open symbols) normal stress differences, N_1 and N_2, as a function of the non-dimensional shear rate $\hat{\dot{\gamma}} = \dot{\gamma}\eta_s / G_0$ at different volume fractions. The lines are the best fits of the data to the Herschel-Bulkley equation: $\sigma/\sigma_y = 1 + 404\hat{\dot{\gamma}}^{0.48\pm0.02}$, $N_1/\sigma_y = 0.1 + 195\hat{\dot{\gamma}}^{0.65\pm0.02}$, $-N_2/\sigma_y = 0.14 + 359\hat{\dot{\gamma}}^{0.63\pm0.02}$ The dashed lines represent the low and high shear rates asymptotic behaviors of σ, N_1, and N_2; note the transition at $\hat{\dot{\gamma}}_0 = 5\times10^{-5}$.

B. Ballistic and diffusive particle motion in SPGs

To analyze the microscopic dynamics of our SPG, we track the position of each particle as a function of time and compute the non-affine displacements by subtracting the contribution

coming from the uniform shear flow. In the following, the results are presented as a function of the time normalized by the hydrodynamic time $\dot{\gamma}^{-1}$: $\tau = \dot{\gamma}^{-1}t$. Note that τ also represents the total macroscopic strain experienced by the SPGs. The way that particles yield depends on the shear rate: at low shear rates, particles show localized yielding, while at high shear rates the motion of the particles is uniform (see videos in Supplementary Materials). Fig. 3A shows the non-affine trajectories of the center of mass of the particles in the simulation box. The trajectories are randomly oriented with respect to the flow direction, indicating that the displacements of the particles are isotropic. Fig. 3B depicts a particular trajectory constructed by following the displacement of a tagged particle for a long time. The spheres represent the successive positions of the tagged particle at times τ. The trajectory consists of blob-like domains corresponding to the temporary residence of the particle locally moving around some particular location, which are separated by necklace strands associated with particle hops. This shows that particles reside most of their time in cages formed by their neighbors and quickly move over significant distances when cages open and rearrange. To quantify these observations, we compute the non-affine mean-squared displacements along the three directions ($\left\langle \Delta r_i^2(t) \right\rangle$, i = x,y,z that are scaled with the average particle radius) and the average mean-squared displacement $\left\langle \Delta r^2(t) \right\rangle$ at different shear rates as a function of time (Fig. S3). The mean-squared displacements $\left\langle \Delta r_i^2(t) \right\rangle$ are all equal, showing that the non-affine particle displacements are isotropic. In Fig. 3C the average mean-squared displacements for $\phi = 0.8$ are plotted as functions of the non-dimensional time τ. Similar results are obtained at all volume fractions. Fig. 3C shows that particle motion is ballistic at short times, i.e. $\left\langle \Delta r^2(\tau) \right\rangle \sim \tau^2$, and diffusive at long times, i.e. $\left\langle \Delta r^2(\tau) \right\rangle \sim \tau$, for all applied shear rates. The crossover τ_m between the two regimes can be

determined in log-log coordinates from the intersection between the short and long-time variations. The values of τ_m depends on both the applied shear rate and volume fraction (Table S2).

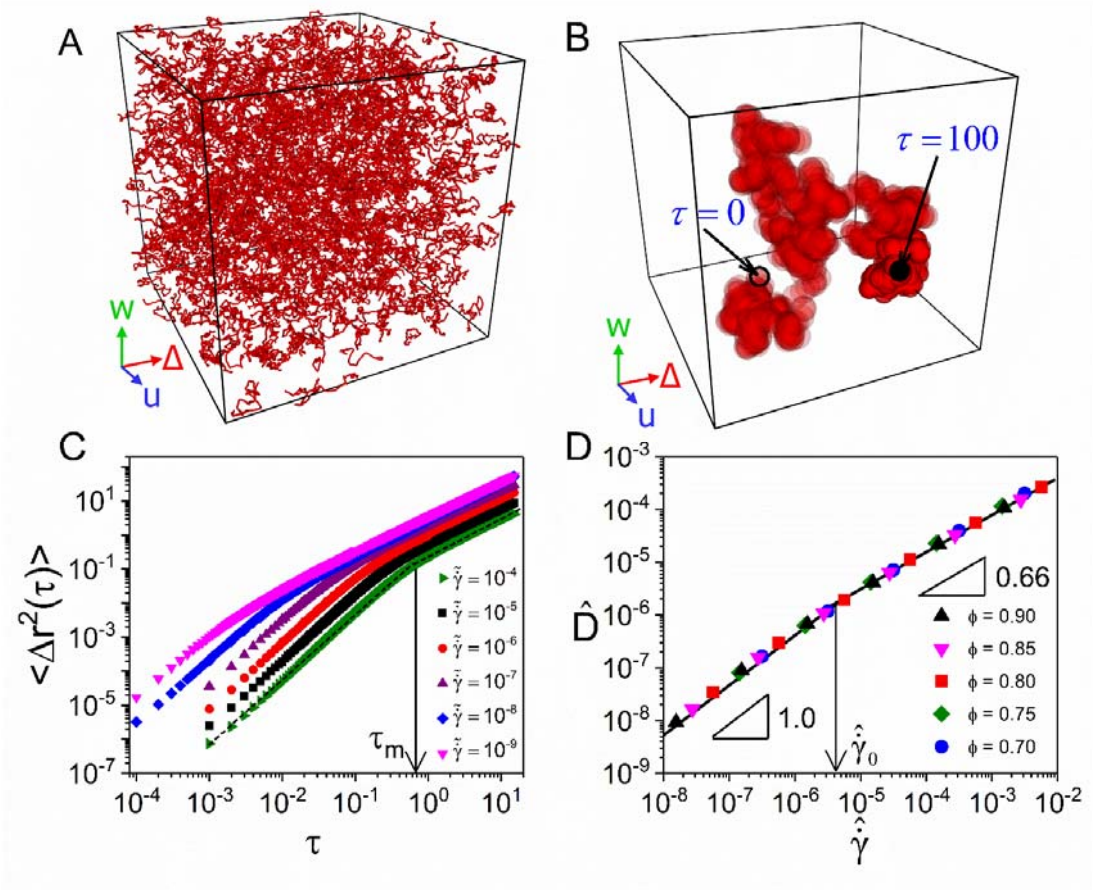

FIG. 3. Non-affine displacements in SPGs. (A) Nonaffine trajectories of all particles in shear flow at a shear rate of $\tilde{\dot{\gamma}} = \dot{\gamma}\eta_s / E^* = 10^{-4}$ for a duration of $\tau = 10$. (B) Non-affine trajectory of a tagged particle. Other particles are not shown; the color of the particle is darker at longest time. (C) Mean-square displacements versus dimensionless time at different shear rates for $\phi = 0.8$. (D) Master curve of the diffusion coefficient $\hat{D} = D\eta_s / R^2 G_0$ as a function of $\hat{\dot{\gamma}}$ obtained for SPGs with different volume fraction. Note the transition at $\hat{\dot{\gamma}}_0 \cong 5\times10^{-5}$.

Note that we have tested a possible dependence of the results on the system size by computing the mean-square displacements when the particle number is varied to a large extent. As shown in Fig. S5, the mean square displacements as a function of time for 125, 1000 and 10,000 particles at 80% volume fraction are essentially the same. The diffusivities at the lowest shear rate of for 125 (L = 8.7), 1000, (L = 17.4), and 10,000 particles (L = 37.4), are, $\tilde{D}/\tilde{\dot{\gamma}} =$ 0.38, 0.49, 0.50, respectively, about a two percent difference between 1000 and 10,000 particles indicating numerical convergence. The short and long time regimes as well as the position of the crossover τ_m are not affected by finite size effects contrary to what has been reported for 2D systems [15, 17, 20].

The long-time diffusion coefficients at different volume fractions can be made non-dimensional as $\hat{D} = D\eta_s / G_0 R^2$ using the scaling factor $G_0 R^2 / \eta_s$. The values computed for different shear rates are listed in Table S3. In Fig. 3D, $\hat{D}$ is plotted versus the non-dimensional shear rate $\hat{\dot{\gamma}} = \dot{\gamma}\eta_s / G_0$ used in the previous section to represent the stress and normal stress differences. The data for the different volume fractions collapse onto a master curve that exhibits two distinct power-law variations at small and large shear rates. At low shear rates, the diffusion coefficient is proportional to the shear rate and varies like $\hat{D} \simeq 0.6\hat{\dot{\gamma}}$. At high shear rates, the diffusion coefficient still increases but with a weaker dependence on the shear rate: $\hat{D} \sim \hat{\dot{\gamma}}^{0.67}$. The crossover between the low and high shear regimes is determined from the intersection between the power-law behaviors at low and high shear rates: $\hat{\dot{\gamma}}_0 \cong 5\times10^{-6}$. It is important to note that this value is the same as the one that marks the crossover between the low shear plateau and the power law regime for the stress and normal stress differences in Fig. 2 A-B.

C. The fluctuating elastic forces

To elucidate the microscopic origin of ballistic motion in SPGs, we consider the normalized autocorrelation function of the elastic force experienced by the particles at contact as a function of time and at different shear rates:

$$C(\tau)=\left\langle \frac{\mathbf{F}(\tau+\tau_0)\cdot\mathbf{F}(\tau_0)}{|\mathbf{F}(\tau_0)|^2}\right\rangle, \tag{5}$$

where $\mathbf{F}(\tau)$ is the elastic force on a particle at time τ and $\left|\mathbf{F}(\tau_0)\right|$ the magnitude of the force fluctuations. We have computed the correlation functions $C(\tau)$ for different shear rates and different volume fractions. The behavior of the force autocorrelation functions for suspensions with a volume fraction of $\phi = 0.8$ are plotted against the dimensional time τ in Fig. 4A. Similar results are obtained for the other volume fractions. The autocorrelation functions $C(\tau)$ decrease with the non-dimensional time τ, the decay being slower at high shear rates. For each force autocorrelation function we define a characteristic decay time $\tau_d\left(\tilde{\dot{\gamma}},\phi\right)$ from $C(\tau_d)=1/e$. The values of τ_d computed at different shear rates for all the volume fractions are listed in Table S2. In Fig. 4B we plot the characteristic time τ_d and the characteristic time τ_m that marks the end of the ballistic regime in Fig. 3C against $\hat{\dot{\gamma}}=\dot{\gamma}\eta_s/G_0$. Both quantities τ_d and τ_m collapse on master curves which are parallel yielding a proportional relationship between τ_d and τ_m : $\tau_m = 1.7\tau_d$. Thus, the duration of the ballistic regime is set by the persistence time of the elastic repulsive force generated when the particles come into contact. This demonstrates that the short time

ballistic motion is associated with the elastic recoil of the contact forces experienced by the particles when they collide. The microscopic times τ_d and τ_m exhibit the same behaviors at low and high shear: for $\hat{\dot{\gamma}} < \hat{\dot{\gamma}}_0$, they increase linearly with the shear rate whereas for $\hat{\dot{\gamma}} > \hat{\dot{\gamma}}_0$ they follow the power law $\tau_d \cong \tau_m \sim \hat{\dot{\gamma}}^{0.25}$.

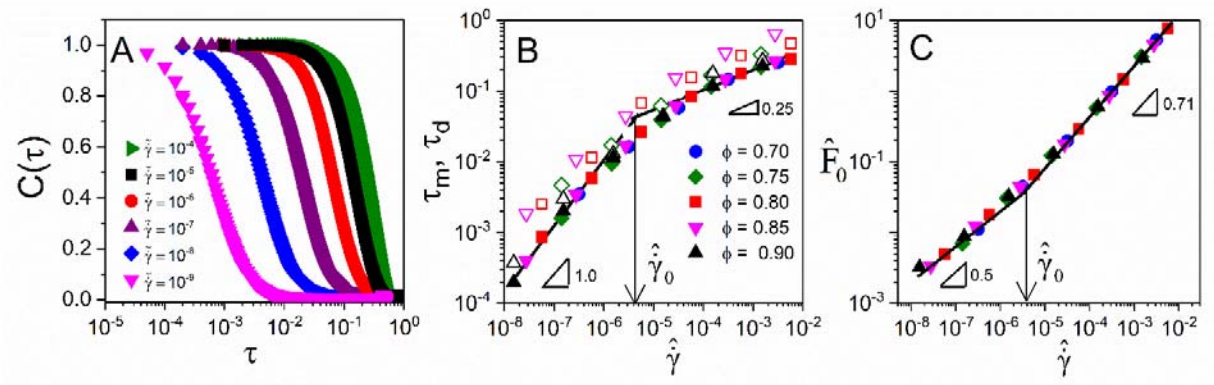

FIG. 4. Properties of the elastic force fluctuations in SPGs. (A) Elastic force autocorrelation function versus dimensionless time at different shear rates ($\phi = 0.8$); (B) Characteristic times τ_m (open symbols) and τ_d (full symbols) versus $\hat{\dot{\gamma}} = \dot{\gamma}\eta_s / G_0$. (C) The amplitude of the force fluctuations, $\hat{F}_0$, as a function of $\hat{\dot{\gamma}}$ obtained for SPGs with different volume fractions. Symbol coding in panels B and C is the same as in Fig. 2D; note the transition at $\hat{\dot{\gamma}}_0 \cong 5\times10^{-5}$.

Let us turn our attention to the magnitude of the force fluctuations. Fig. 4C shows that the values of the non-dimensional quantity $\hat{F}_0 = |\mathbf{F}(\tau_0)| / G_0 R^2$ for different volume fractions collapse when they are plotted against the dimensionless shear rate $\hat{\dot{\gamma}} = \dot{\gamma}\eta_s / G_0$ already used in Fig. 2A-B and Fig. 3D (see also Table S2). This result exemplifies the important role of the bulk elasticity and confirms that $\hat{\dot{\gamma}} = \dot{\gamma}\eta_s / G_0$ is the parameter that controls the microscopic dynamics of SPGs. $\hat{F}_0$ exhibits two different variations depending again on the value of the shear rate with respect with $\hat{\dot{\gamma}}_0$: at low shear rates we have $\hat{F}_0 \sim \hat{\dot{\gamma}}^{0.5}$ whereas $\hat{F}_0 \sim \hat{\dot{\gamma}}^{0.71}$ at high shear rates.

D. Microstructural relaxation

We return to our observation that trajectories of individual particles are spatially heterogeneous with particles rattling in localized regions before hopping over large distances (Figs. 2A-B). To quantify this observation, we characterize the timescales that particles spend in their cage using the incoherent intermediate scattering function (ISF):

$$F_s(\mathbf{k},\tau) = \frac{1}{N}\left\langle \sum_{j=1}^{N} \exp\left[i\mathbf{k}\cdot\left(\mathbf{r}_j(\tau) - \mathbf{r}_j(0)\right)\right]\right\rangle, \tag{6}$$

where $\mathbf{k}$ is a spatial wave vector and N is the total number of the particles in the simulation. We compute the ISF at different volume fractions and shear rates at a wave vector $kR = 4.0$, which is close to the position of the first peak of the structure factor and corresponds to the cage size (Fig. S5). The variations of the ISFs at different shear rates versus the non-dimensional time τ are shown in Fig. 5A for $\phi = 0.8$. The ISFs exhibit a plateau at short time due to the caging of the particles in their local environment before they start rearranging, which is followed by a decay because of the non-affine motion of the particles. At all volume fractions, the decay of the ISF is nearly exponential, and we can determine a microstructure relaxation time τ_c from $F_s(k,\tau_c) = 1/e$. The results are plotted against the non-dimensional shear rate $\hat{\dot{\gamma}}$ in Fig. 5B. The characteristic relaxation times form a master curve that has the form of the Herschel-Bulkley equation $\tau_c = \tau_0 + k\hat{\dot{\gamma}}^n$. The yield value $\tau_0 = \dot{\gamma} t_0 = \gamma_0$ can be interpreted as the total strain experienced by the particles before they escape their cage. Its value of 0.13 corresponds to deformation above which thermal systems melt, which matches the Lindemann criterion[43, 44]

. The crossover between the yield plateau and the power-law variation of τ_c also occurs at $\hat{\dot{\gamma}}_0 \simeq 5\times10^{-6}$, which limits the low and high shear rate regimes defined above. Interestingly the inset of Fig. 5B shows that the characteristic quantity τ_c is a unique function of the persistence time τ_d, indicating that cage escape is also controlled by the fluctuating elastic forces. We have repeated the same analysis for larger values of *kR*. The Herschel-Bulkley shape is preserved with nearly the same exponent; the yield value increases when *kR* decreases because the characteristic distance over which we follow the motion of the particles increases (see Fig. S6).

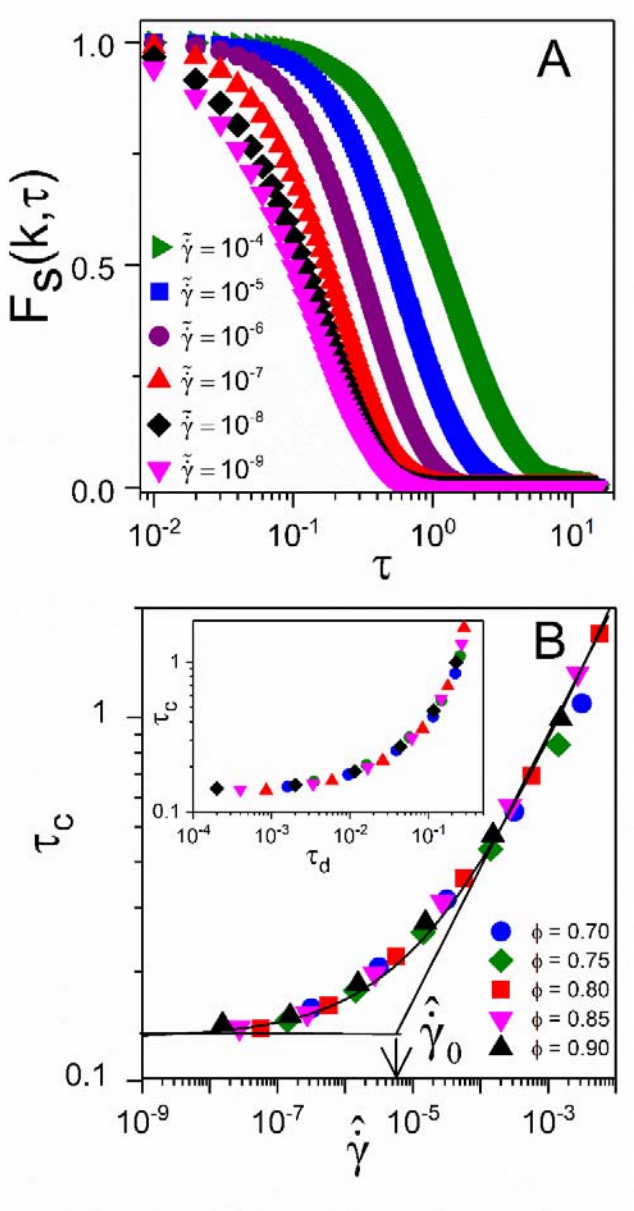

FIG. 5. Microstructural relaxation in SPGs. (A) Intermediate scattering function versus dimensionless time computed at different shear rates $\tilde{\dot{\gamma}}$ (kR = 4.0, $\phi = 0.8$). (B) Master curve of the microstructural relaxation time τ_c as a function of $\hat{\dot{\gamma}} = \dot{\gamma}\eta_s / G_0$. The line is a fit of the data to a Herschel-Bulkley form equation ($\tau_c = 0.132 + 15.5\hat{\dot{\gamma}}^{0.44\pm0.02}$). The dashed lines represent the low and high shear rates asymptotic behaviors of τ_c; note the transition at $\hat{\dot{\gamma}}_0 \cong 5\times10^{-5}$. Inset: τ_c as a function of τ_d.

IV. Discussion

A. Short time microscopic dynamics of SPGs

On the basis of our results we can now propose a physical understanding of the three-dimensional microscopic dynamics of athermal jammed suspensions interacting through a soft elastic potential. When particles collide at short times, they adjust their shape and distort the cage where they are trapped until an imbalance in the elastic force causes the particles to move in a ballistic fashion. Ballistic motion has also been found in simulations of various athermal glassy materials [13, 15, 16, 18, 20, 24]. Here we have demonstrated that the duration of the ballistic motion (τ_m) is set by the persistence time of the elastic forces (τ_d) associated with the shear-induced cage deformation, which can be quantified by the force autocorrelation function. In this description the elastic kicks experienced by the particles create a mechanical noise that is responsible for non-affine particle motion. At short time particles rattle around fixed positions but when the cumulated strain exceeds a value τ_c, particles leave their transient cage and hop to another location where they become trapped for another period of time. The characteristic time τ_c plays the role of a microstructural relaxation time. Interestingly it is also set by the persistence time of the elastic forces τ_d. Thus, the persistence time of the fluctuating elastic force, τ_d, appears to be the elementary clock that governs the microscopic dynamics of SPGs.

B. Long time microscopic dynamics of SPGs

Since particles are continuously interacting with their neighbors in all directions, they experience an isotropic series of ballistic events, ultimately leading to particle diffusive motion at long times. The shear-induced diffusion coefficient of SPGs is described by two scaling forms. The scaling found at low shear rates when $\hat{\dot{\gamma}} = \dot{\gamma}\eta_s / G_0 < 5\times10^{-6}$ ($\hat{D} \simeq 0.6\hat{\dot{\gamma}}$) is the same as the one

that governs the shear-induced diffusion of hard particles in unjammed suspensions, although the driving mechanisms (long-ranged hydrodynamic interactions versus near-field elastohydrodynamics) are different [45, 46]. At high shear rates when $\hat{\dot{\gamma}} = \dot{\gamma}\eta_s / G_0 > 5\times10^{-6}$, the diffusion coefficient exhibits a sublinear dependence on the shear rate: $\hat{D} \sim \hat{\dot{\gamma}}^{0.67}$. Power-law variations $\hat{D} \sim \hat{\dot{\gamma}}^{m}$ of the shear-induced diffusion coefficient with a variety of exponents have been reported in experiments [6] for hard-sphere glasses (m = 0.8) and computer simulations [10, 15-17] of two-dimensional Lennard-Jones (m = 0.5) and foams ($m \cong 2/3$ and 0.5).

In SPGs we can relate the non-trivial dependence of the diffusion coefficient on the shear rate to the properties of the fluctuating elastic forces in the framework of equilibrium statistical physics. We use the Green-Kubo relationship that relates the diffusion coefficient to the velocity fluctuations: $D = \frac{1}{3}\int_0^\infty \langle V(0)V(t)\rangle dt$. Since the force and velocity are proportional through the mobility coefficient, the velocity must remain correlated during the characteristic time τ_d, and $\hat{V}_0$ and $\hat{F}_0$ are proportional through the mobility coefficient, which does not depend on the shear rate, i.e. $\hat{V}_0 = M\hat{F}_0$. We then obtain in non-dimensional units:

$$\hat{D} = \frac{1}{3} M^2 \hat{F}_0^{\,2} \tau_d \hat{\dot{\gamma}}^{-1}. \qquad (7)$$

This relation shows that the shear-induced diffusion coefficient is related to the short time dynamics of the particles through the amplitude and the correlation time of the elastic forces they experience at contact. Replacing $\hat{F}_0$ and τ_d by their power-law variations at low ($\hat{F}_0 \sim \hat{\dot{\gamma}}^{0.5}$, $\tau_d \sim \hat{\dot{\gamma}}$) and high ($\hat{F}_0 \sim \hat{\dot{\gamma}}^{0.71}$, $\tau_d \sim \hat{\dot{\gamma}}^{0.25}$,) shear rates, we recover that $\hat{D} \sim \hat{\dot{\gamma}}$ and $\hat{D} \sim \hat{\dot{\gamma}}^{0.67}$, respectively, which are the results found in Fig. 2D from the mean-squared displacements data.

Thus, shear-induced diffusion in SPGs is connected to the magnitude of the elastic contact forces and the elastically-driven, short-time, ballistic motion of the particles.

An interesting consequence is that the shear induced diffusion coefficient $\hat{D}$ can also be related to the microstructural relaxation time τ_c. In Fig. 6A we plot the diffusion coefficients $\hat{D}$ computed for different volume fractions against the microstructural relaxation time τ_c. All the data collapse on a master curve demonstrating the connection between shear-induced diffusivity and local relaxation. For reference, we have also plotted the prediction obtained from the ISF for a Gaussian distribution of displacement (Fickian diffusion): $\tau_c = \hat{\dot{\gamma}}/\hat{k}^2\hat{D}$, with $\hat{k} = kR$. The latter solution is in reasonable agreement with the data computed at all shear rates, suggesting that the spatial heterogeneities associated with the short time displacements do not significantly affect the long-time behavior in SPGs.

C. Connecting microscopic dynamics and macroscopic rheology

In this section we bridge the gap between the microscopic dynamics and the macroscopic rheology and we derive several the relationships that relate σ, N_1 and N_2 to τ_c. Let us first focus our attention on the shear stress σ. In a steady-state sheared system, the energy supplied to the system has to be dissipated. The elastic forces being dominant [4], we express the energy dissipation as $\sigma\dot{\gamma} = n\langle \mathbf{F}.\mathbf{V} \rangle$, where n is the number density of particles ($n = 3\phi/4\pi R^3$; ϕ: volume fraction; R: particle radius), $\mathbf{F}$ and $\mathbf{V}$ are the elastic force acting on the particles and the velocity, which are proportional. Since $\hat{V}_0 = M\hat{F}_0$, we have in dimensionless form:

$$\frac{\sigma}{\sigma_y} = \frac{3}{4\pi}\frac{\phi M\hat{F}_0^{\,2}}{\gamma_y\hat{\dot{\gamma}}}, \tag{8}$$

where $\sigma_y = G_0\gamma_y$ is the yield stress, γ_y being the yield strain. Relation (8) has two important consequences. First, since the ratio ϕ/γ_y is constant (Table 1), it justifies that the shear stresses computed for different volume fractions must be described by a generic flow curve when they are scaled by the yield stress σ_y and plotted as a function of the dimensionless shear rate $\hat{\dot{\gamma}} = \dot{\gamma}\eta_s/G_0$. Second, it establishes a link between the macroscopic stress and the short time dynamics of the particles, which is further supported by the similar functional form observed between τ_c and σ in Fig. 2 and Fig. 5B.

We now establish the relationships that link together the microstructural relaxation time τ_c and the macroscopic stress σ. In the Herschel-Bulkley equation, the shear stress is the sum of the yield stress arising from the cage elasticity G_0 ($\sigma_y = G_0\gamma_y$, γ_y is the yield strain) and an excess elastic term originating from shear-induced rearrangements [4]. Similarly, the non-dimensional relaxation time τ_c (or equivalently the macroscopic strain) can be decomposed into a yield value τ_0 and an excess contribution. Since the stress is of elastic origin, we assume that the excess quantities $\sigma - \sigma_y$ and $\tau_c - \tau_0$ are related through the low-frequency modulus as: $\sigma - \sigma_y = G_0(\tau_c - \tau_0)$. After rearranging, we obtain:

$$\frac{\sigma - \sigma_y}{\sigma_y} = \frac{\tau_0}{\gamma_y}\frac{(\tau_c - \tau_0)}{\tau_0}, \tag{9}$$

In Fig. 6B, we plot the normalized excess shear stress $(\sigma - \sigma_y)/\sigma_y$ against the normalized excess relaxation time $(\tau_c - \tau_0)/\tau_0$. The data computed at different volume fractions collapse onto a single curve that is close to the expected linear variation. The exponent is slightly larger than one because of the small difference between the Herschel-Bulkley

exponents for the flow curves and relaxation time. Figs. 6C and 6D suggest that similar relations exist for the first and second normal stress differences. This is somewhat surprising a priori since the normal stress differences only involve elasticity whereas the shear stress is associated with energy dissipation as expresses by Eqs 8-9. This correspondence may come from the fact that normal stress differences originate from the contact forces between the particles and are proportional to the shear stress [4].

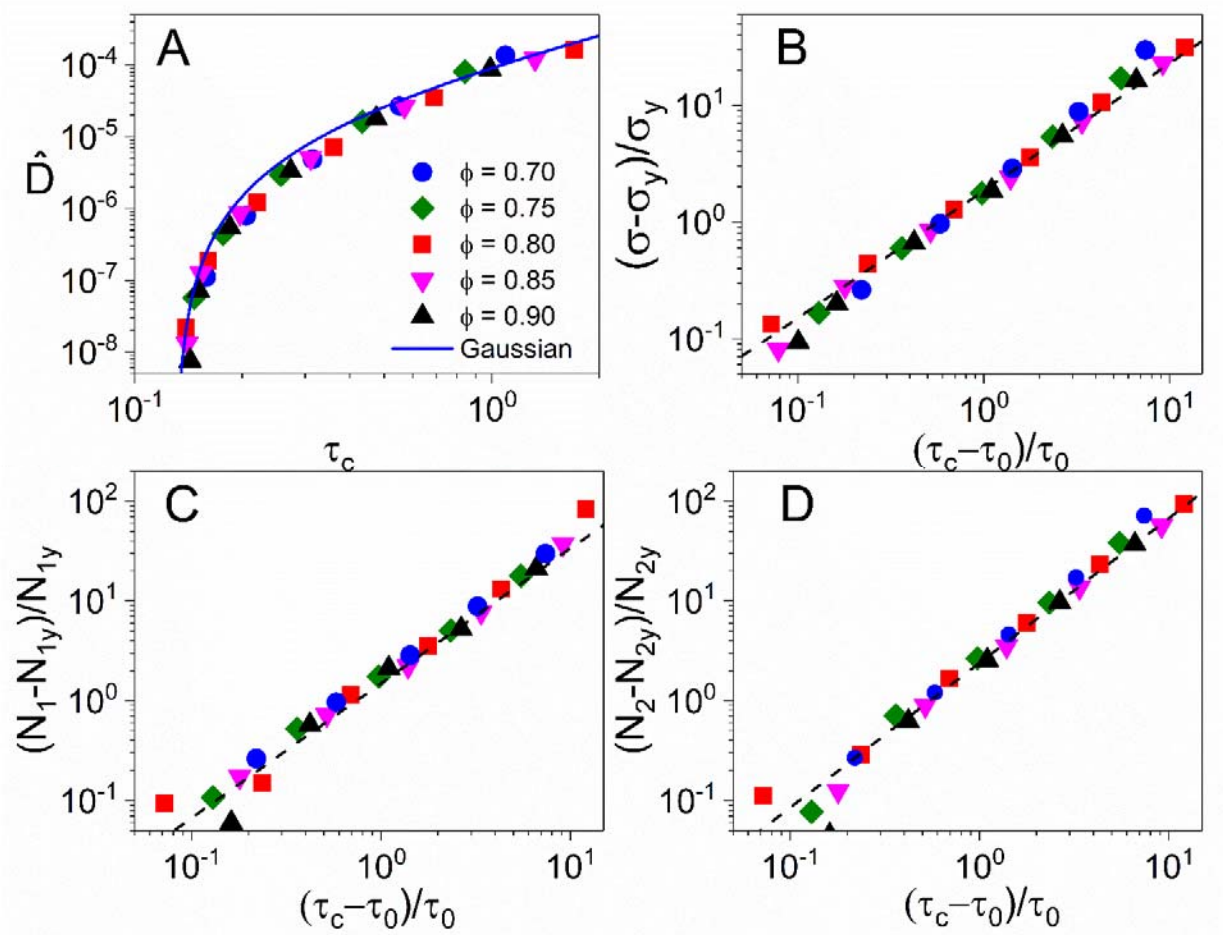

FIG. 6. Predicting diffusivity and macroscopic rheology from the structural relaxation time. (A) Master curve of the scaled diffusion coefficient as a function of the structural relaxation time. The blue line represents the Gaussian solution $\hat{D} = \hat{\dot{\gamma}} / R^2 k^2 \, \tau_c = 1.24 \times 10^{-4} \left(\tau_c - \tau_0 \right)^{2.27} / \tau_c$. (B) Master curve of the normalized excess shear stress versus the normalized excess structural time. The dashed line is a power-law fit to the data: $(\sigma - \sigma_y)/\sigma_y = 1.86 \left[(\tau_c - \tau_0)/\tau_0 \right]^{1.08 \pm 0.04}$. (C) and (D) Master curves of the normalized excess normal stress differences. The dashed lines are a power-law fits to the data:

$(N_1 - N_{1y})/N_{1y} = 1.50\left[(\tau_c - \tau_0)/\tau_0\right]^{1.35\pm0.04}$ and $(N_2 - N_{2y})/N_{2y} = 2.40\left[(\tau_c - \tau_0)/\tau_0\right]^{1.45\pm0.04}$. N_{1y} and N_{2y} are the yield values of the first and normal stress differences.

V. Concluding remarks and perspectives

Our simulations provide a physical understanding of the three-dimensional microscopic dynamics of athermal jammed suspensions interacting through a soft potential. At short times particles experience shear-induced collisions which distort their shape and cause an imbalance in the elastic forces, forcing the particles to move in a ballistic fashion. The elastic kicks experienced by the particles thus create a mechanical noise that is responsible for the particle scale dynamics. At long times particles leave their transient cage and hop to another position where they become trapped for another period of time. The dynamical sequence of localized cage motion and activated hopping exhibit similarities with the behavior of thermal systems like supercooled liquids [47, 48] and hard sphere glasses [49].

The connection between the properties of the non-affine particle trajectories, the contact force statistics, and the macroscopic rheology of SPGs has been rationalized in terms of a hierarchy of characteristic times. τ_d characterizes the persistence time of the net elastic force experienced by the particles during collisions; it plays a key role since its constitute the elementary clock that controls the entire sequence of dynamical processes taking place in SPGs. τ_m marks the crossover between ballistic motion at short times and shear-induced diffusion at long times; it has the same order of magnitude as τ_d as shown in Fig. 4B. τ_c is a structural relaxation time that represents the residence time of the particles in their local environment before they hop on another position. τ_c scales with τ_d as shown in the inset of Fig. 5B but it is much larger than τ_d showing that the particles bounces several against their neighbors before

hopping to another position. τ_c gives access to the long-time diffusion coefficient, the shear stress and the first and second normal stress differences through a set of scaling relations presented in Fig 6. In the literature a few conflicting results have been reported about the connection between the macroscopic rheology and microscopic relaxation processes in hard suspensions and two-dimensional foams [6, 7, 10]. Here we demonstrate that the structural relaxation time τ_c can be utilized as a tool to determine the macroscopic rheology of soft jammed colloids. This poses the question of the practical determination of τ_c in experiments. τ_c is accessible through the decay of the ISF function, which in colloidal systems can be measured using real space videomicroscopy experiments [6]. Orthogonal superposition rheometry has also been used to probe in-cage to out-of-cage motion transition [50, 51]. Optical techniques based on microscopy or light scattering offer promising perspectives to probe the local dynamics of soft materials like SPGs [51, 52].

Bailey et al. show [53] data for avalanches that are system size dependent, but they do not report results on diffusivity under shear, thus we cannot make a direct comparison. It is also of note that the potential used there is a realistic potential for metallic glasses but is different from ours. The problem of dynamical heterogeneities in microgel suspensions which are known to interact through Hertzian potentials has been addressed experimentally [54]. The authors report that the number of fast particles involved in cooperative regions decreases dramatically away from the jamming transition around maximum packing. Indeed the number of particles involved around a volume fraction of 69% is about the same as the average number of contacts between particles, indicating that the cooperative region is close to the size of the cage of nearest neighbors surrounding a specific particle. It is beyond the scope of this paper, but certainly

future work is warranted to understand the details on why the system presented here does not show a size dependence for diffusivity.

Our results exemplify the importance of the particle softness. Indeed the magnitude and decay time of the fluctuating elastic force are determined by the particle elasticity and the elastic deformation experienced by the particles when they are jammed above close-packing. We thus believe that our findings apply to a broad class of jammed suspensions made of soft repulsive particles such as emulsions, microgels, or vesicles. The universal scaling shown in Fig. 2 has already been reported in concentrated microgel suspensions and emulsions [1, 4, 41]. Of particular interest is the value of the Herschel-Bulkley exponent of the shear stress which is close to 0.5 in fairly good agreement with experimental data for different materials such as concentrated emulsions [1, 4], microgels [1, 4, 33, 41, 54-56], and vesicles [57]. There are far less data available for the normal stress differences. Two sets of data have reported. They both report first and second normal stress differences of opposite signs described by Herschel-Bulkley equations. However in one set of data normal stress differences and shear stress are proportional in agreement with our findings [1, 4] whereas in the other a quadratic dependence is reported [58]. However soft interactions in colloids may be more diverse for instance when particles interpenetrate or experience osmotic deswelling [2]. In the near future it would be interesting to extend the present model to particles with different sources of softness.

The shear induced diffusion coefficient and the macroscopic shear stress are related to the magnitude and decay time of the fluctuating elastic force in the framework of equilibrium statistical mechanics. An important consequence is that these quantities are all universal functions of the unique dimensionless variable $\hat{\dot{\gamma}} = \dot{\gamma}\eta_s / G_0$. The scaling behavior of these dynamical properties give evidence for two flow regimes separated by a broad crossover around

$\hat{\dot{\gamma}}_0$. The value of the crossover is set by the condition that the characteristic time τ_d or equivalently the macroscopic strain is equal to the yield strain γ_y (see Fig. 4C). Thus, at low shear rates, the advection time $1/\dot{\gamma}$ is much longer than the structural relaxation time τ_d and the force autocorrelation decays before the particles yield macroscopically. Yielding events are expected to be intermittent and particles to have enough time to relax to local equilibrium before the flow induces a new rearrangement. On the opposite, at high shear rates particles yield macroscopically before the force autocorrelation has vanished so that they continuously yield and never find local equilibrium positions. These predictions echo to a recent investigation of the rate dependence local motion and of spatiotemporal correlations in 3D flows of soft solids [12]. Preliminary results which are shown in the Supplementary Materials (see videos) prompt for further investigation in the near future.

Supplementary materials

See supplementary material for supporting information discussed in the main text.

Acknowledgment

FK and RTB gratefully acknowledge financial support from the National Science Foundation (MRSEC under award number DMR- 1720595).

References

1. Bonnecaze, R.T. and M. Cloitre, *Micromechanics of Soft Particle Glasses*, in *High Solid Dispersions*, M. Cloitre, Editor. 2010, Springer Berlin Heidelberg: Berlin, Heidelberg. p. 117-161.
2. Vlassopoulos, D. and M. Cloitre, *Tunable Rheology of Dense Soft Deformable Colloids.* Curr. Opin. Colloid Interface Sci., 2014. **19**(6): p. 561-574.
3. Bonn, D., M.M. Denn, L. Berthier, T. Divoux, and S. Manneville, *Yield Stress Materials in Soft Condensed Matter.* Rev. Mod. Phys., 2017. **89**(3): p. 035005.
4. Seth, J.R., L. Mohan, C. Locatelli-Champagne, M. Cloitre, and R.T. Bonnecaze, *A Micromechanical Model to Predict the Flow of Soft Particle Glasses.* Nat. Mater., 2011. **10**(11): p. 838-843.
5. Schall, P., D.A. Weitz, and F. Spaepen, *Structural Rearrangements That Govern Flow in Colloidal Glasses.* Science, 2007. **318**(5858): p. 1895.
6. Besseling, R., E.R. Weeks, A. Schofield, and W. Poon, *Three-Dimensional Imaging of Colloidal Glasses under Steady Shear.* Phys. Rev. Lett., 2007. **99**(2): p. 028301.
7. Möbius, M.E., G. Katgert, and M. Van Hecke, *Relaxation and Flow in Linearly Sheared Two-Dimensional Foams.* EPL (Europhysics Letters), 2010. **90**(4): p. 44003.
8. Eisenmann, C., C. Kim, J. Mattsson, and D.A. Weitz, *Shear Melting of a Colloidal Glass.* Phys. Rev. Lett., 2010. **104**(3): p. 035502.
9. Nordstrom, K.N., J.P. Gollub, and D.J. Durian, *Dynamical Heterogeneity in Soft-Particle Suspensions under Shear.* Physical Review E, 2011. **84**(2): p. 021403.
10. Sexton, M., M. Möbius, and S. Hutzler, *Bubble Dynamics and Rheology in Sheared Two-Dimensional Foams.* Soft Matter, 2011. **7**(23): p. 11252-11258.
11. Sentjabrskaja, T., P. Chaudhuri, M. Hermes, W. Poon, J. Horbach, S. Egelhaaf, and M. Laurati, *Creep and Flow of Glasses: Strain Response Linked to the Spatial Distribution of Dynamical Heterogeneities.* Scientific reports, 2015. **5**: p. 11884.
12. Vasisht, V.V., S.K. Dutta, E. Del Gado, and D.L. Blair, *Rate Dependence of Elementary Rearrangements and Spatiotemporal Correlations in the 3d Flow of Soft Solids.* Phys. Rev. Lett., 2018. **120**(1): p. 018001.
13. Ono, I.K., S. Tewari, S.A. Langer, and A.J. Liu, *Velocity Fluctuations in a Steadily Sheared Model Foam.* Phys. Rev. E, 2003. **67**(6): p. 061503.
14. Lemaître, A. and C. Caroli, *Plastic Response of a Two-Dimensional Amorphous Solid to Quasistatic Shear: Transverse Particle Diffusion and Phenomenology of Dissipative Events.* Phys. Rev. E, 2007. **76**(3): p. 036104.
15. Lemaître, A. and C. Caroli, *Rate-Dependent Avalanche Size in Athermally Sheared Amorphous Solids.* Phys. Rev. Lett., 2009. **103**(6): p. 065501.
16. Tsamados, M., *Plasticity and Dynamical Heterogeneity in Driven Glassy Materials.* Eur. Phys. J. A, 2010. **32**(2): p. 165-181.

17. Martens, K., L. Bocquet, and J.-L. Barrat, *Connecting Diffusion and Dynamical Heterogeneities in Actively Deformed Amorphous Systems.* Phys. Rev. Lett., 2011. **106**(15): p. 156001.
18. Ferrero, E.E., K. Martens, and J.-L. Barrat, *Relaxation in Yield Stress Systems through Elastically Interacting Activated Events.* Phys. Rev. Lett., 2014. **113**(24): p. 248301.
19. Maloney, C., *Avalanches and Diffusion in Bubble Rafts.* EPL (Europhysics Letters), 2015. **111**(2): p. 28001.
20. Roy, A.P., K. Karimi, and C.E. Maloney, *Rheology, Diffusion, and Velocity Correlations in the Bubble Model.* arXiv preprint arXiv:1508.00810, 2015.
21. Hébraud, P. and F. Lequeux, *Mode-Coupling Theory for the Pasty Rheology of Soft Glassy Materials.* Phys. Rev. Lett., 1998. **81**(14): p. 2934.
22. Lin, J. and M. Wyart, *Microscopic Processes Controlling the Herschel-Bulkley Exponent.* Phys. Rev. E, 2018. **97**(1): p. 012603.
23. Rahmani, Y., K. Van Der Vaart, B. Van Dam, Z. Hu, V. Chikkadi, and P. Schall, *Dynamic Heterogeneity in Hard and Soft Sphere Colloidal Glasses.* Soft Matter, 2012. **8**(15): p. 4264-4270.
24. Gnan, N. and E. Zaccarelli, *The Microscopic Role of Deformation in the Dynamics of Soft Colloids.* Nat. Phys., 2019(15): p. 683–688.
25. Seth, J.R., M. Cloitre, and R.T. Bonnecaze, *Elastic Properties of Soft Particle Pastes.* J. Rheol., 2006. **50**(3): p. 353-376.
26. Liu, T., F. Khabaz, R.T. Bonnecaze, and M. Cloitre, *On the Universality of the Flow Properties of Soft-Particle Glasses.* Soft Matter, 2018. **14**(34): p. 7064-7074.
27. Khabaz, F., M. Cloitre, and R.T. Bonnecaze, *Structural State Diagram of Concentrated Suspensions of Jammed Soft Particles in Oscillatory Shear Flow.* Phys. Rev. Fluids, 2018. **3**(3): p. 033301.
28. Khabaz, F., T. Liu, M. Cloitre, and R.T. Bonnecaze, *Shear-Induced Ordering and Crystallization of Jammed Suspensions of Soft Particles Glasses.* Phys. Rev. Fluids, 2017. **2**(9): p. 093301.
29. Mohan, L., C. Pellet, M. Cloitre, and R. Bonnecaze, *Local Mobility and Microstructure in Periodically Sheared Soft Particle Glasses and Their Connection to Macroscopic Rheology.* J. Rheol., 2013. **57**(3): p. 1023-1046.
30. Lubachevsky, B.D. and F.H. Stillinger, *Geometric Properties of Random Disk Packings.* J. Stat. Phys., 1990. **60**(5): p. 561-583.
31. Stillinger, F.H. and B.D. Lubachevsky, *Crystalline—Amorphous Interface Packings for Disks and Spheres.* J. Stat. Phys., 1993. **73**(3): p. 497-514.
32. Borrega, R., M. Cloitre, I. Betremieux, B. Ernst, and L. Leibler, *Concentration Dependence of the Low-Shear Viscosity of Polyelectrolyte Micro-Networks: From Hard Spheres to Soft Microgels.* Europhys. Lett., 1999. **47**(6): p. 729-735.
33. Pellet, C. and M. Cloitre, *The Glass and Jamming Transitions of Soft Polyelectrolyte Microgel Suspensions.* Soft Matter, 2016. **12**(16): p. 3710-3720.
34. Liu, K.K., D.R. Williams, and B.J. Briscoe, *The Large Deformation of a Single Micro-Elastomeric Sphere.* J. Phys. D: Appl. Phys., 1998. **31**(3): p. 294.
35. Phillips, R.J., J.F. Brady, and G. Bossis, *Hydrodynamic Transport Properties of Hard□Sphere Dispersions. I. Suspensions of Freely Mobile Particles.* Phys. Fluids, 1988. **31**(12): p. 3462-3472.

36. Lees, A.W. and S.F. Edwards, *The Computer Study of Transport Processes under Extreme Conditions.* J. Phys. C: Solid State Phys., 1972. **5**(15): p. 1921-1928.
37. Plimpton, S., *Fast Parallel Algorithms for Short-Range Molecular Dynamics.* J. Comput. Phys., 1995. **117**(1): p. 1-19.
38. Larson, R.G., *The Structure and Rheology of Complex Fluids*. 1999, New York: Oxford Univ. Press.
39. Rogers, S.A., B.M. Erwin, D. Vlassopoulos, and M. Cloitre, *A Sequence of Physical Processes Determined and Quantified in Laos: Application to a Yield Stress Fluid.* Journal of Rheology, 2011. **55**(2): p. 435-458.
40. Larson, R.G., *The Elastic Stress in "Film Fluids".* J. Rheol., 1997. **41**(2): p. 365-372.
41. Cloitre, M., R. Borrega, F. Monti, and L. Leibler, *Glassy Dynamics and Flow Properties of Soft Colloidal Pastes.* Phys. Rev. Lett., 2003. **90**(6): p. 068303.
42. Siebenbürger, M., M. Fuchs, H. Winter, and M. Ballauff, *Viscoelasticity and Shear Flow of Concentrated, Noncrystallizing Colloidal Suspensions: Comparison with Mode-Coupling Theory.* J. Rheol., 2009. **53**(3): p. 707-726.
43. Zhou, Y., M. Karplus, K.D. Ball, and R.S. Berry, *The Distance Fluctuation Criterion for Melting: Comparison of Square-Well and Morse Potential Models for Clusters and Homopolymers.* J. Chem. Phys., 2002. **116**(5): p. 2323-2329.
44. Lindemann, F.A., Phys. Z., 1910(11): p. 609.
45. Qiu, X., H.D. Ou-Yang, D. Pine, and P. Chaikin, *Self-Diffusion of Interacting Colloids Far from Equilibrium.* Phys. Rev. Lett., 1988. **61**(22): p. 2554.
46. Nott, P.R. and J.F. Brady, *Pressure-Driven Flow of Suspensions: Simulation and Theory.* J. Fluid Mech., 1994. **275**: p. 157-199.
47. Schweizer, K.S., *Derivation of a Microscopic Theory of Barriers and Activated Hopping Transport in Glassy Liquids and Suspensions.* J. Chem. Phys., 2005. **123**(24): p. 244501.
48. Chaudhuri, P., L. Berthier, and W. Kob, *Universal Nature of Particle Displacements Close to Glass and Jamming Transitions.* Phys. Rev. Lett., 2007. **99**(6): p. 060604.
49. Weeks, E.R., J.C. Crocker, A.C. Levitt, A. Schofield, and D.A. Weitz, *Three-Dimensional Direct Imaging of Structural Relaxation near the Colloidal Glass Transition.* Science, 2000. **287**(5453): p. 627-631.
50. Jacob, A.R., A.S. Poulos, S. Kim, J. Vermant, and G. Petekidis, *Convective Cage Release in Model Colloidal Glasses.* Phys. Rev. Lett., 2015. **115**(21): p. 218301.
51. Aime, S., L. Ramos, and L. Cipelletti, *Microscopic Dynamics and Failure Precursors of a Gel under Mechanical Load.* Proc. Natl. Acad. Sci. U. S. A., 2018. **115**(14): p. 3587-3592.
52. Knowlton, E.D., D.J. Pine, and L. Cipelletti, *A Microscopic View of the Yielding Transition in Concentrated Emulsions.* Soft Matter, 2014. **10**(36): p. 6931-6940.
53. Bailey, N.P., J. Schiøtz, A. Lemaître, and K.W. Jacobsen, *Avalanche Size Scaling in Sheared Three-Dimensional Amorphous Solid.* Phys. Rev. Lett., 2007. **98**(9): p. 095501.
54. Nordstrom, K.N., E. Verneuil, P. Arratia, A. Basu, Z. Zhang, A.G. Yodh, J.P. Gollub, and D.J. Durian, *Microfluidic Rheology of Soft Colloids above and Below Jamming.* Phys. Rev. Lett., 2010. **105**(17): p. 175701.
55. Bécu, L., S. Manneville, and A. Colin, *Yielding and Flow in Adhesive and Nonadhesive Concentrated Emulsions.* Phys. Rev. Lett., 2006. **96**(13): p. 138302.
56. Paredes, J., M.A. Michels, and D. Bonn, *Rheology across the Zero-Temperature Jamming Transition.* Phys. Rev. Lett., 2013. **111**(1): p. 015701.

57. Fujii, S. and W. Richtering, *Size and Viscoelasticity of Spatially Confined Multilamellar Vesicles.* Eur. Phys. J. E: Soft Matter Biol. Phys., 2006. **19**(2): p. 139-148.
58. De Cagny, H., M. Fazilati, M. Habibi, M.M. Denn, and D. Bonn, *The Yield Normal Stress.* J. Rheol., 2019. **63**(2): p. 285-290.

Supplementary Materials

Particle Dynamics Predicts Shear Rheology of Soft Particle Glasses

Fardin Khabaz,[1] Michel Cloitre[2] and Roger T. Bonnecaze[1*]

[1]McKetta Department of Chemical Engineering, The University of Texas at Austin,

Austin, TX, 78712, USA

[2]Molecular, Macromolecular Chemistry, and Materials, ESPCI Paris, CNRS, PSL University,

10 Rue Vauquelin, 75005 Paris, France

[*]Corresponding author e-mail: rtb@che.utexas.edu

Table of contents

Supplementary figures

Supplementary tables

Supplementary videos

Movie S1. Displacement field of suspensions with a volume fraction of $\phi = 0.8$ at a high shear rate of $\tilde{\dot{\gamma}} = 10^{-4}$. The interval time of $\Delta\tau = 0.01$ is used to track the particles over a duration of $\tau = 10.0$

Movie S2. Displacement field of suspensions with a volume fraction of $\phi = 0.8$ at a low shear rate of $\tilde{\dot{\gamma}} = 10^{-8}$. The interval time of $\Delta\tau = 0.01$ is used to track the particles over a duration of $\tau = 10.0$

Figure S1

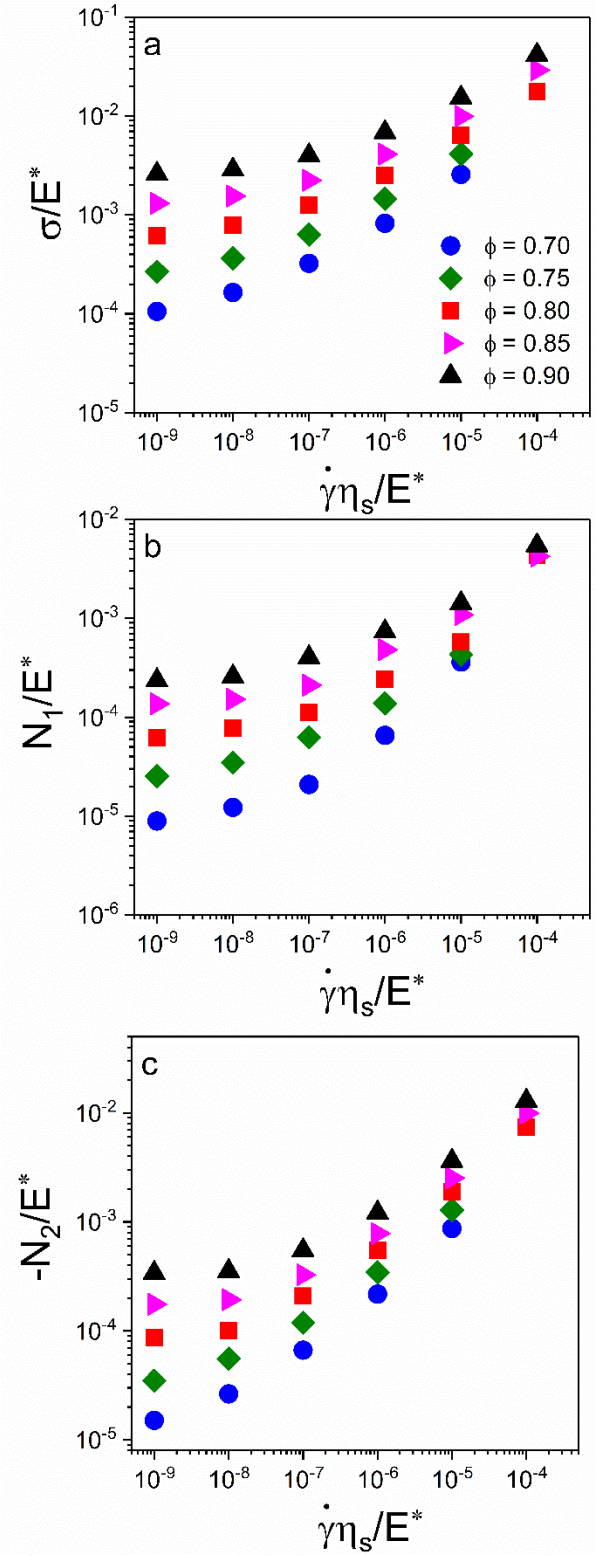

FIG S1: (a) Shear stress, (b) first and (c) second normal stress differences as a function of the dimensionless shear rate $\tilde{\dot{\gamma}} = \dot{\gamma}\eta_s / E^*$ for SPGs with $\phi = 0.70, 75, 0.80, 0.85, \text{and } 0.90$. The data are listed in Table S1 below. The continuous lines show the best fits to the Herschel-Bulkley equation. Data for $\phi = 0.70 \text{ and } 0.75$ at the highest shear rate are not shown because the suspensions crystallize.

Figure S2

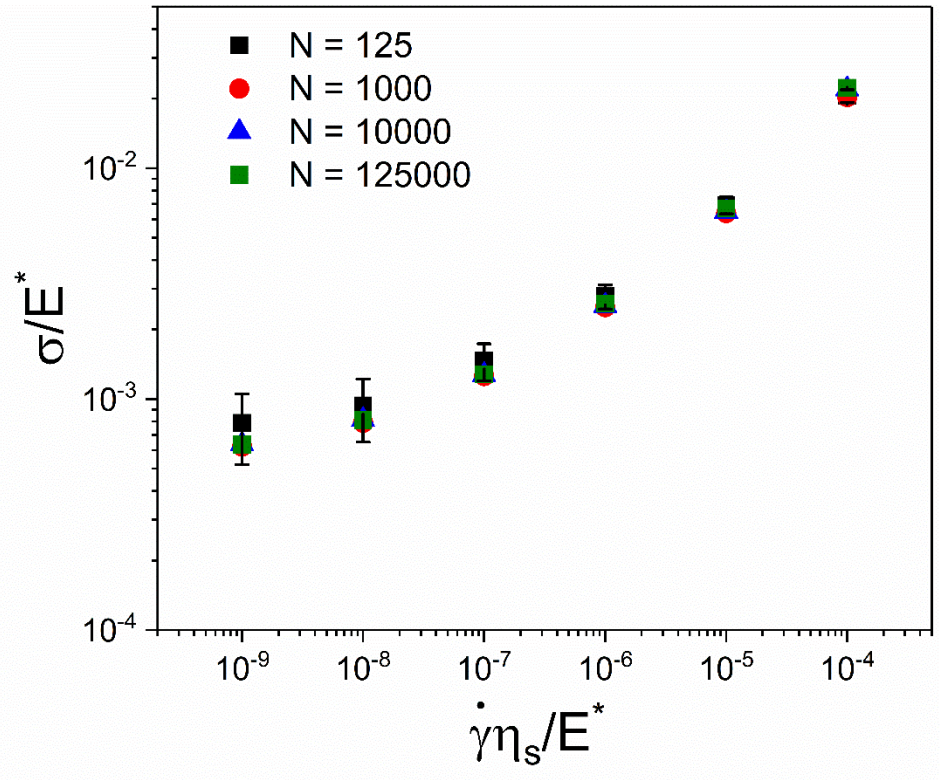

FIG S2: Flow curves computed for a suspension with different particle numbers at volume fraction of 0.80.

Figure S3

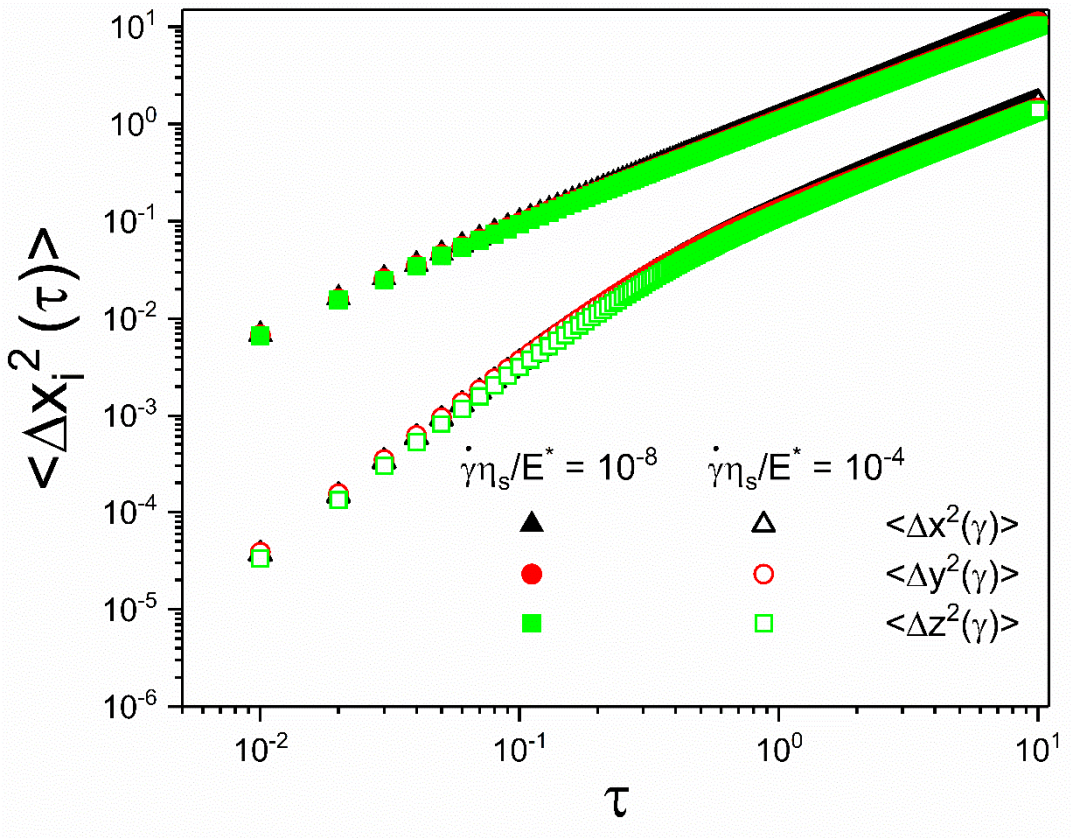

Fig. S3: Three component of the mean-square displacements versus dimensionless time at low (filled symbols) and high (open symbols) shear rates for SPG with volume fraction of 0.9. The diffusion coefficients ($\tilde{D} = D\eta_S / R^2 E^*$) obtained in x, y, and z directions at low shear rates are 6.3×10^{-9}, 5.7×10^{-9}, and 5.3×10^{-9} and at high shear rates are 8.3×10^{-6}, 7.4×10^{-6}, and 7.1×10^{-6}, respectively.

Figure S4

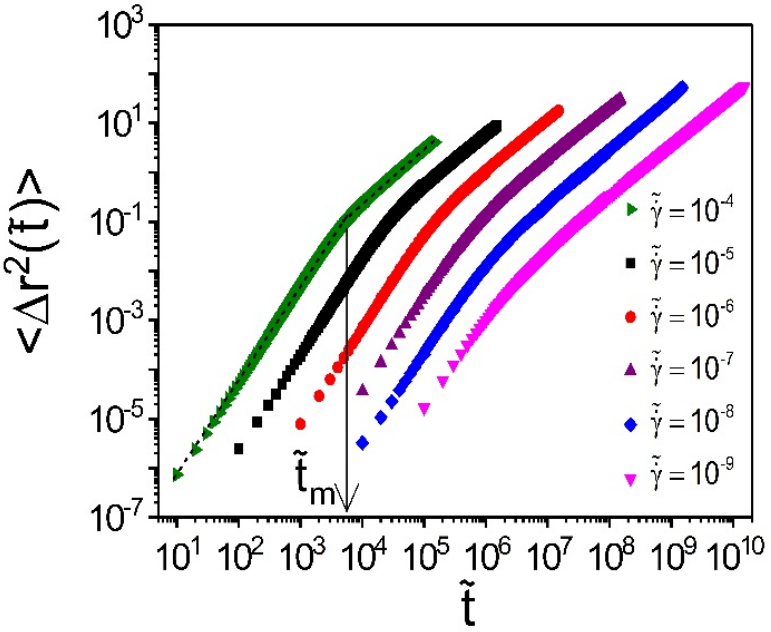

FIG. S4. Mean square displacement as function of the normalized time $\tilde{t} = t\eta_S / E^*$ obtained at different shear rates for a SPG with a volume fraction of 0.8. $\tilde{t}_m$ marks the crossover between the short time ballistic regime and the long time diffusive regime.

Figure S5

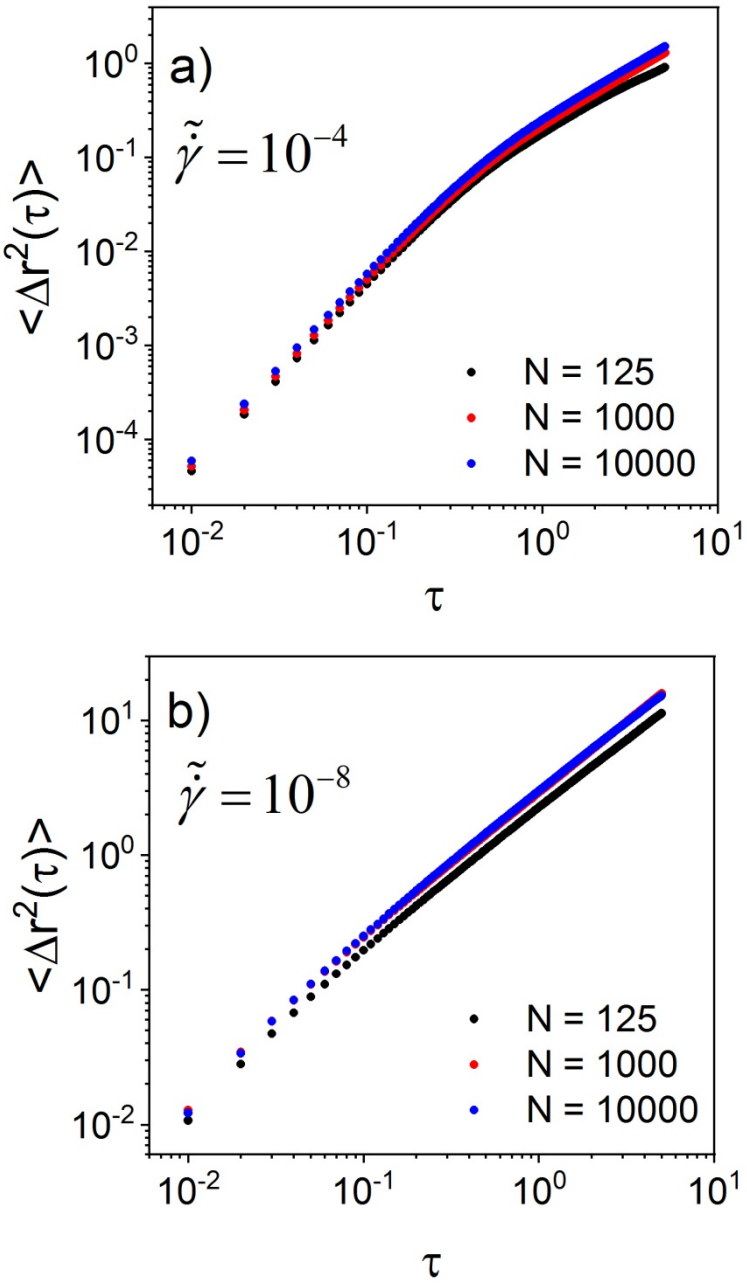

FIG S5. Mean-squared displacement as a function of dimensionless time at (a) high and (b) low shear rates for suspensions with different number of particles at volume fraction of 0.8. The long time diffusion coefficients ($\tilde{D} = D\eta_S / R^2 E^*$) for $N = 125$, 1000, 10000 are: a) $\tilde{D} / \tilde{\dot{\gamma}} =$ 3.7×10^{-2}, 3.8×10^{-2}, 4.4×10^{-2}; b) $\tilde{D} / \tilde{\dot{\gamma}} = 0.38$, 0.49, 0.50.

Figure S6

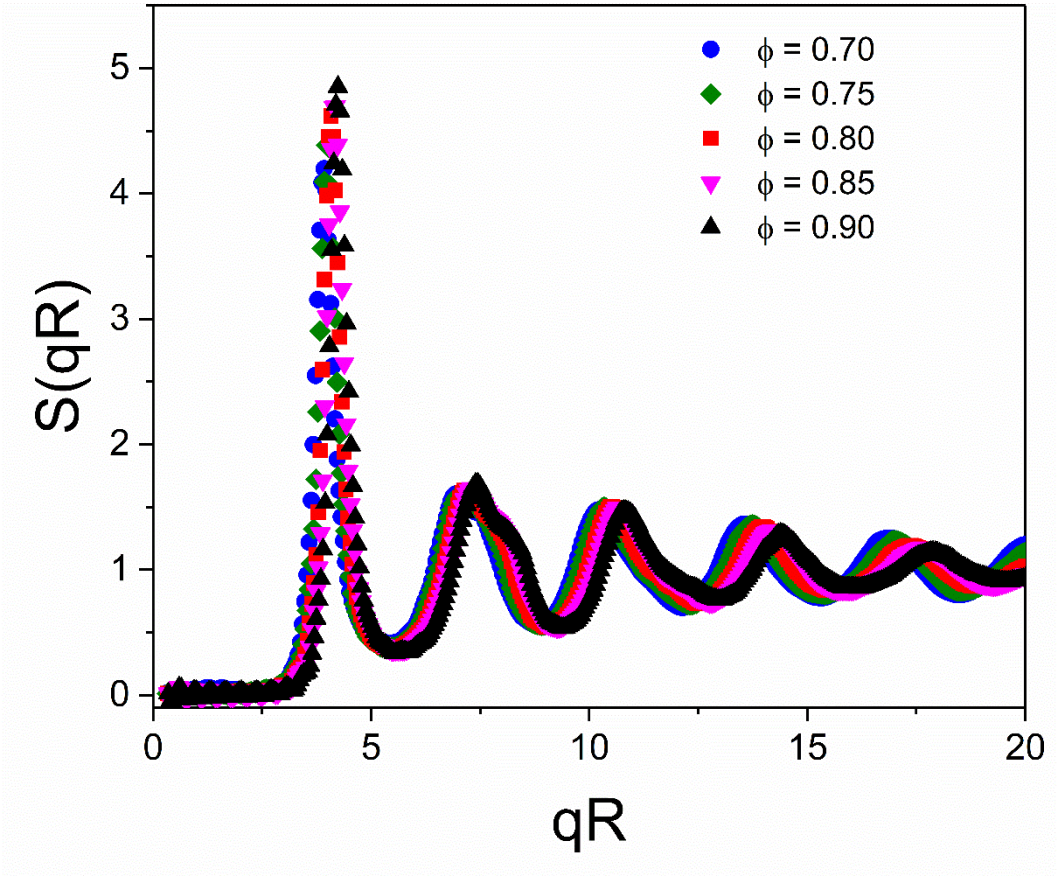

Fig. S6: Structure factor obtained at quiescent condition for suspensions with different volume fractions.

Figure S7

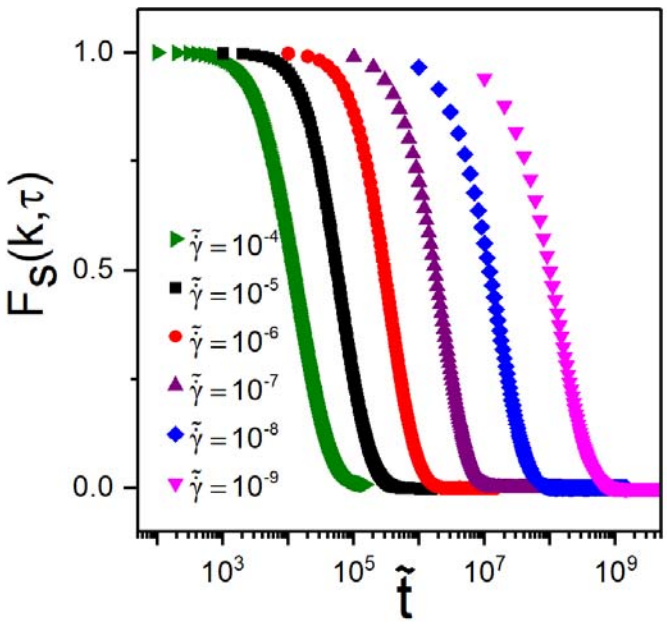

FIG S7. Intermediate scattering function as function of the normalized time $\tilde{t} = t\eta_S / E^*$ obtained at different shear rates for a SPG with a volume fraction of 0.8.

Figure S8

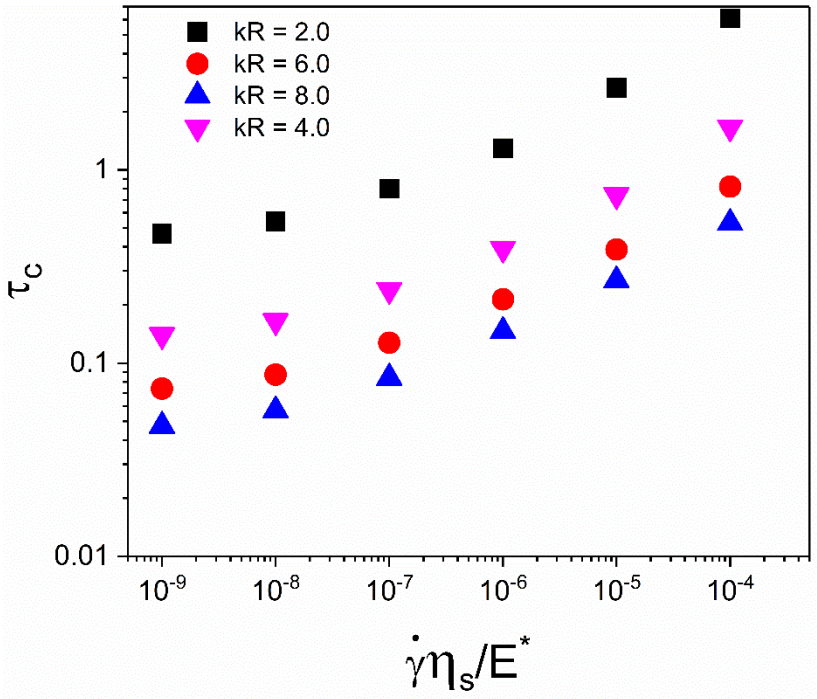

FIG S8. Values of the microscopic relaxation time (τ_C) obtained at different *kR* values for a suspension with a volume fraction of 0.8.

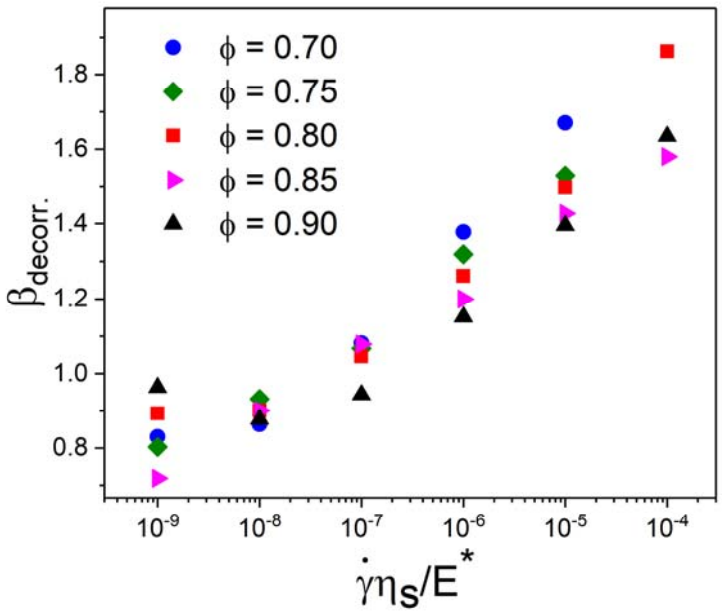

FIG S9. Values of the exponent β obtained from fitting the elastic force autocorrelation to $f(\tau) = \exp\left(-(\tau/\tau_d)^{\beta}\right)$ as a function of the shear rate for suspensions with different volume fractions.

TABLE S1: Variations of the shear stress (σ/E^*), first (N_1/E^*) and second normal ($-N_2/E^*$) stress computed at different shear rates.

$\dot{\gamma}\eta_s/E^*$	σ/E^*	N_1/E^*	$-N_2/E^*$
	$\phi = 0.70$		
10^{-5}	2.57×10^{-3}	3.61×10^{-4}	8.67×10^{-4}
10^{-6}	8.23×10^{-4}	6.53×10^{-5}	2.17×10^{-4}
10^{-7}	3.24×10^{-4}	2.09×10^{-5}	6.68×10^{-5}
10^{-8}	1.65×10^{-4}	1.22×10^{-5}	2.64×10^{-5}
10^{-9}	1.06×10^{-4}	8.89×10^{-6}	1.51×10^{-5}
	$\phi = 0.75$		
10^{-5}	4.14×10^{-3}	4.30×10^{-4}	1.28×10^{-3}
10^{-6}	1.46×10^{-3}	1.38×10^{-4}	3.45×10^{-4}
10^{-7}	6.34×10^{-4}	6.27×10^{-5}	1.19×10^{-4}
10^{-8}	3.65×10^{-4}	3.46×10^{-5}	5.55×10^{-5}
10^{-9}	2.67×10^{-4}	2.52×10^{-5}	3.50×10^{-5}
	$\phi = 0.80$		
10^{-4}	1.77×10^{-2}	4.07×10^{-3}	7.46×10^{-3}
10^{-5}	6.39×10^{-3}	5.76×10^{-4}	1.89×10^{-3}
10^{-6}	2.50×10^{-3}	2.42×10^{-4}	5.47×10^{-4}
10^{-7}	1.26×10^{-3}	1.11×10^{-4}	2.09×10^{-4}
10^{-8}	7.90×10^{-4}	7.73×10^{-5}	1.00×10^{-4}
10^{-9}	6.23×10^{-4}	6.17×10^{-5}	8.67×10^{-5}
	$\phi = 0.85$		
10^{-4}	2.91×10^{-2}	4.20×10^{-3}	9.92×10^{-3}
10^{-5}	9.94×10^{-3}	1.08×10^{-3}	2.52×10^{-3}
10^{-6}	4.11×10^{-3}	4.79×10^{-4}	7.82×10^{-4}
10^{-7}	2.24×10^{-3}	2.11×10^{-4}	3.26×10^{-4}
10^{-8}	1.55×10^{-3}	1.51×10^{-4}	1.94×10^{-4}
10^{-9}	1.31×10^{-3}	1.36×10^{-4}	1.75×10^{-4}
	$\phi = 0.90$		
10^{-4}	4.15×10^{-2}	5.43×10^{-3}	1.29×10^{-2}
10^{-5}	1.53×10^{-2}	1.41×10^{-3}	3.62×10^{-3}
10^{-6}	6.83×10^{-3}	7.30×10^{-4}	1.21×10^{-3}
10^{-7}	3.97×10^{-3}	4.00×10^{-4}	5.47×10^{-4}
10^{-8}	2.86×10^{-3}	2.57×10^{-4}	3.54×10^{-4}
10^{-9}	2.60×10^{-3}	2.35×10^{-4}	3.38×10^{-4}

TABLE S2: Crossover time (τ_m) between the ballistic and diffusive regimes, relaxation time of the elastic force (τ_d), and non-dimensional amplitude of the force fluctuations, $\hat{F}_0$, computed at different shear rates.

$\dot{\gamma}\eta_s/E^*$	τ_m	τ_d	$\hat{F}_0$
	$\phi = 0.70$		
10^{-5}	0.3549	0.2523	5.3216
10^{-6}	0.2290	0.1466	0.9877
10^{-7}	0.0951	0.0575	0.1965
10^{-8}	0.0251	0.0163	0.0444
10^{-9}	0.0080	0.0035	0.0111
	$\phi = 0.75$		
10^{-5}	0.3332	0.2201	3.0362
10^{-6}	0.1669	0.1149	0.5706
10^{-7}	0.0613	0.0388	0.1215
10^{-8}	0.0169	0.0095	0.0306
10^{-9}	0.0047	0.0016	0.0069
	$\phi = 0.80$		
10^{-4}	0.4704	0.2847	7.7072
10^{-5}	0.3209	0.1771	1.4805
10^{-6}	0.1565	0.0841	0.2880
10^{-7}	0.0677	0.0262	0.0655
10^{-8}	0.0113	0.0059	0.0177
10^{-9}	0.0025	0.0009	0.0050
	$\phi = 0.85$		
10^{-4}	0.6433	0.2666	4.5723
10^{-5}	0.3490	0.1466	0.8596
10^{-6}	0.1545	0.0615	0.1774
10^{-7}	0.0441	0.0168	0.0445
10^{-8}	0.0107	0.0039	0.0123
10^{-9}	0.0018	0.0004	0.0034
	$\phi = 0.90$		
10^{-4}	0.2710	0.2250	2.9294
10^{-5}	0.1790	0.1170	0.5879
10^{-6}	0.0443	0.0435	0.1285
10^{-7}	0.0130	0.0115	0.0321
10^{-8}	0.0030	0.0020	0.0087
10^{-9}	0.00037	0.0002	0.0032

TABLE S3: Long-time diffusion coefficient ($D\eta_s/R^2E^*$) computed at different shear rates.

$\dot{\gamma}\eta_s/E^*$	$D\eta_s/R^2E^*$
$\phi = 0.70$	
10^{-5}	6.38×10^{-7}
10^{-6}	1.26×10^{-7}
10^{-7}	2.25×10^{-8}
10^{-8}	3.72×10^{-9}
10^{-9}	5.21×10^{-10}
$\phi = 0.75$	
10^{-5}	8.08×10^{-7}
10^{-6}	1.61×10^{-7}
10^{-7}	2.94×10^{-8}
10^{-8}	4.42×10^{-9}
10^{-9}	5.71×10^{-10}
$\phi = 0.80$	
10^{-4}	4.58×10^{-6}
10^{-5}	9.91×10^{-7}
10^{-6}	1.99×10^{-7}
10^{-7}	3.41×10^{-8}
10^{-8}	5.27×10^{-9}
10^{-9}	6.09×10^{-10}
$\phi = 0.85$	
10^{-4}	5.62×10^{-6}
10^{-5}	1.21×10^{-6}
10^{-6}	2.31×10^{-7}
10^{-7}	3.96×10^{-8}
10^{-8}	5.74×10^{-9}
10^{-9}	6.00×10^{-10}
$\phi = 0.90$	
10^{-4}	7.02×10^{-6}
10^{-5}	1.44×10^{-6}
10^{-6}	2.69×10^{-7}
10^{-7}	4.36×10^{-8}
10^{-8}	5.73×10^{-9}
10^{-9}	6.05×10^{-10}

TABLE S4: Microstructural relaxation time (τ_C) computed at different shear rates.

$\dot{\gamma}\eta_s / E^*$	τ_C
$\phi = 0.70$	
10^{-5}	1.09209
10^{-6}	0.55138
10^{-7}	0.31524
10^{-8}	0.20551
10^{-9}	0.15855
$\phi = 0.75$	
10^{-5}	0.84224
10^{-6}	0.43394
10^{-7}	0.25666
10^{-8}	0.17703
10^{-9}	0.14685
$\phi = 0.80$	
10^{-4}	1.70187
10^{-5}	0.68995
10^{-6}	0.3606
10^{-7}	0.22017
10^{-8}	0.16076
10^{-9}	0.13934
$\phi = 0.85$	
10^{-4}	1.32167
10^{-5}	0.56946
10^{-6}	0.31083
10^{-7}	0.19723
10^{-8}	0.1533
10^{-9}	0.1402
$\phi = 0.90$	
10^{-4}	0.98994
10^{-5}	0.47455
10^{-6}	0.27303
10^{-7}	0.18481
10^{-8}	0.15105
10^{-9}	0.14307

Supplementary Materials

Particle Dynamics Predicts Shear Rheology of Soft Particle Glasses

Fardin Khabaz,[1] Michel Cloitre[2] and Roger T. Bonnecaze[1*]

[1]McKetta Department of Chemical Engineering, The University of Texas at Austin,

Austin, TX, 78712, USA

[2]Molecular, Macromolecular Chemistry, and Materials, ESPCI Paris, CNRS, PSL University,

10 Rue Vauquelin, 75005 Paris, France

[*]Corresponding author e-mail: rtb@che.utexas.edu

Table of contents

Supplementary figures

Supplementary tables

Supplementary videos

Movie S1. Displacement field of suspensions with a volume fraction of $\phi = 0.8$ at a high shear rate of $\tilde{\dot{\gamma}} = 10^{-4}$. The interval time of $\Delta\tau = 0.01$ is used to track the particles over a duration of $\tau = 10.0$

Movie S2. Displacement field of suspensions with a volume fraction of $\phi = 0.8$ at a low shear rate of $\tilde{\dot{\gamma}} = 10^{-8}$. The interval time of $\Delta\tau = 0.01$ is used to track the particles over a duration of $\tau = 10.0$

Figure S1

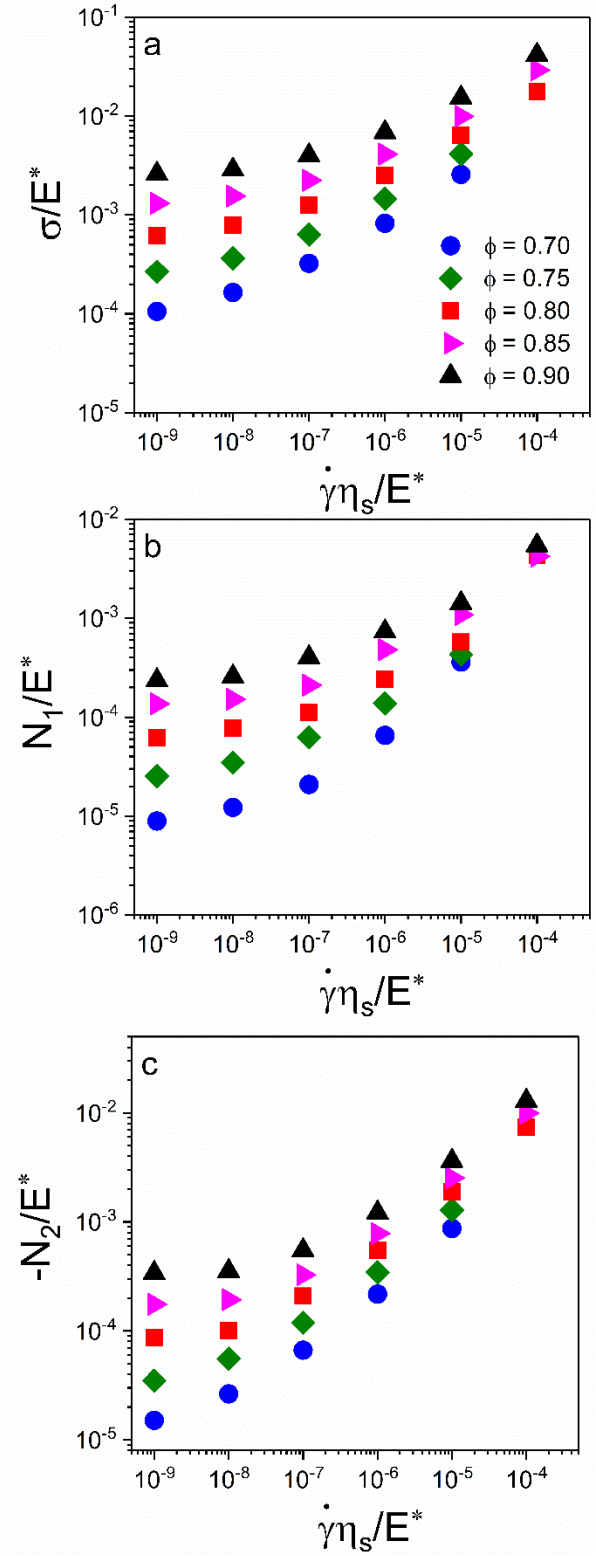

FIG S1: (a) Shear stress, (b) first and (c) second normal stress differences as a function of the dimensionless shear rate $\tilde{\dot{\gamma}} = \dot{\gamma}\eta_s / E^*$ for SPGs with $\phi = 0.70, 75, 0.80, 0.85, \text{and } 0.90$. The data are listed in Table S1 below. The continuous lines show the best fits to the Herschel-Bulkley equation. Data for $\phi = 0.70 \text{ and } 0.75$ at the highest shear rate are not shown because the suspensions crystallize.

Figure S2

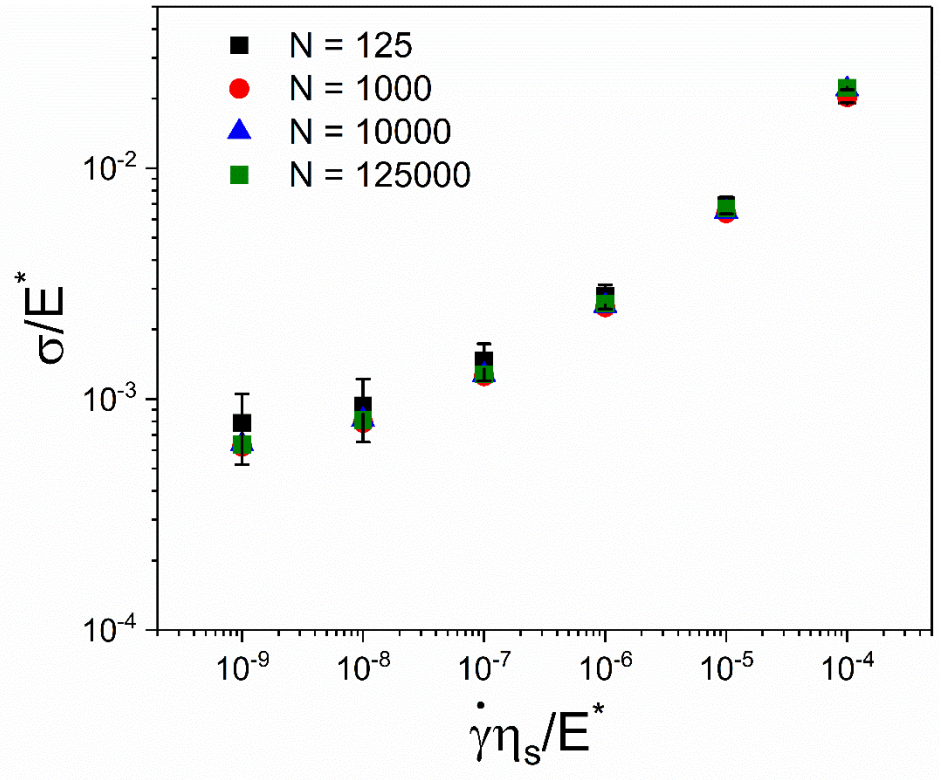

FIG S2: Flow curves computed for a suspension with different particle numbers at volume fraction of 0.80.

Figure S3

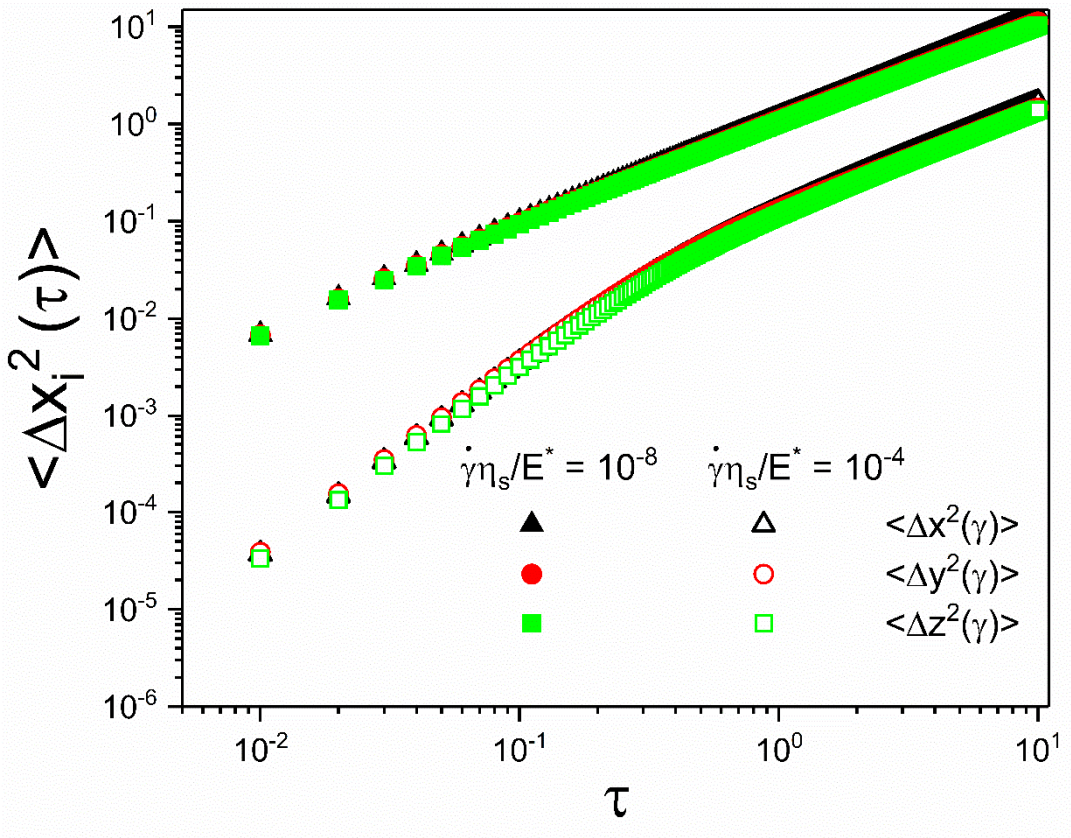

Fig. S3: Three component of the mean-square displacements versus dimensionless time at low (filled symbols) and high (open symbols) shear rates for SPG with volume fraction of 0.9. The diffusion coefficients ($\tilde{D} = D\eta_S / R^2 E^*$) obtained in x, y, and z directions at low shear rates are 6.3×10^{-9}, 5.7×10^{-9}, and 5.3×10^{-9} and at high shear rates are 8.3×10^{-6}, 7.4×10^{-6}, and 7.1×10^{-6}, respectively.

Figure S4

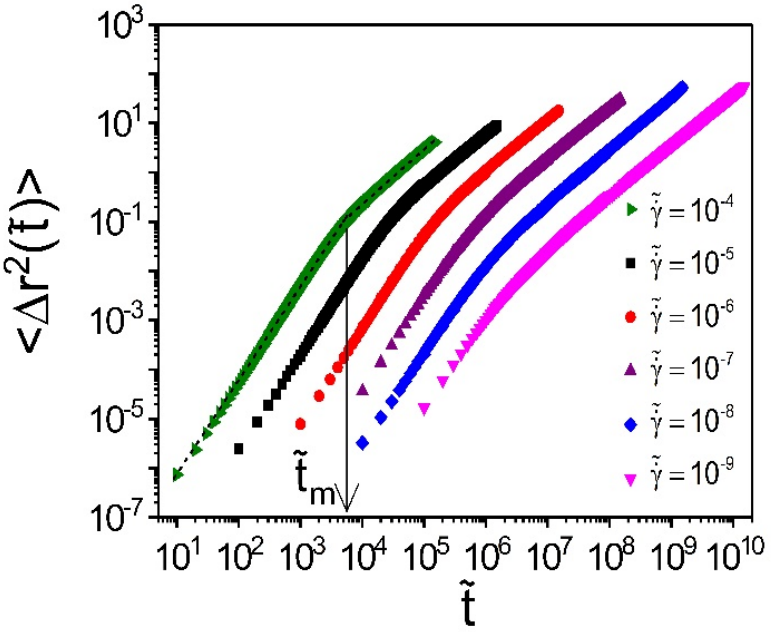

FIG. S4. Mean square displacement as function of the normalized time $\tilde{t} = t\eta_S / E^*$ obtained at different shear rates for a SPG with a volume fraction of 0.8. $\tilde{t}_m$ marks the crossover between the short time ballistic regime and the long time diffusive regime.

Figure S5

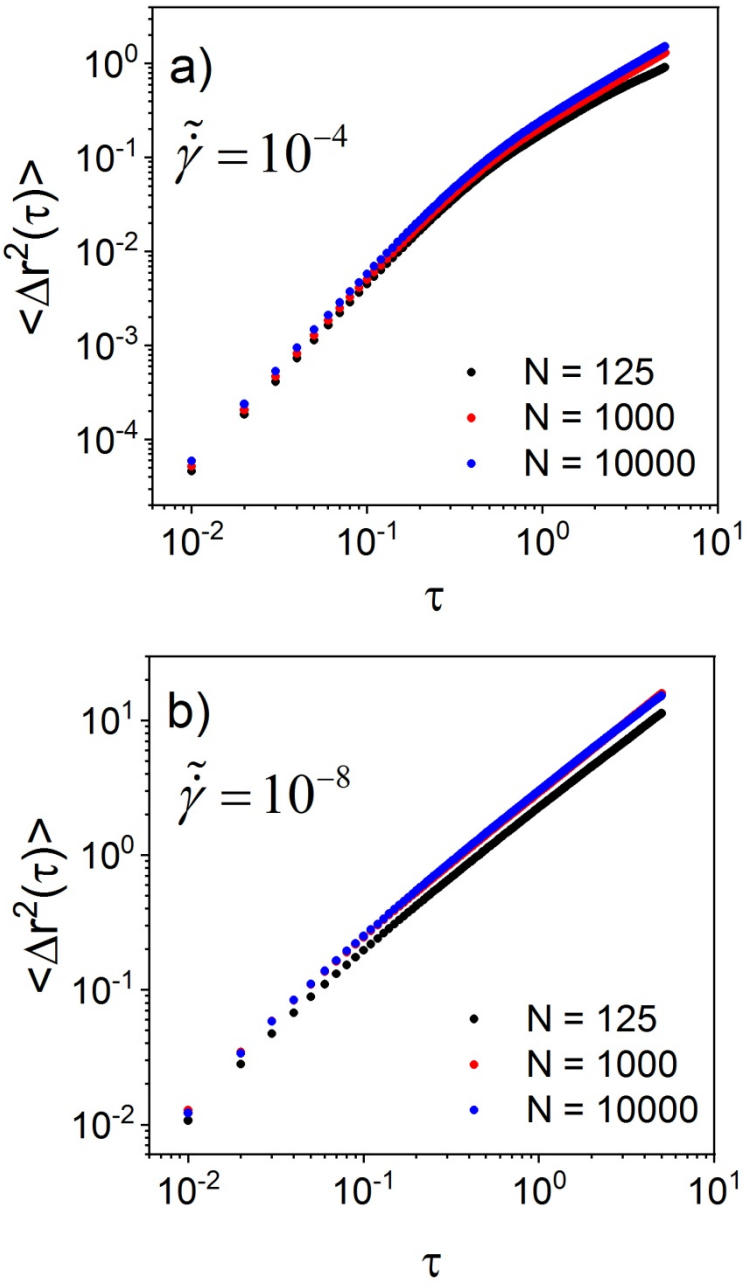

FIG S5. Mean-squared displacement as a function of dimensionless time at (a) high and (b) low shear rates for suspensions with different number of particles at volume fraction of 0.8. The long time diffusion coefficients ($\tilde{D} = D\eta_S / R^2 E^*$) for $N = 125$, 1000, 10000 are: a) $\tilde{D} / \tilde{\dot{\gamma}} =$ 3.7×10^{-2}, 3.8×10^{-2}, 4.4×10^{-2}; b) $\tilde{D} / \tilde{\dot{\gamma}} = 0.38$, 0.49, 0.50.

Figure S6

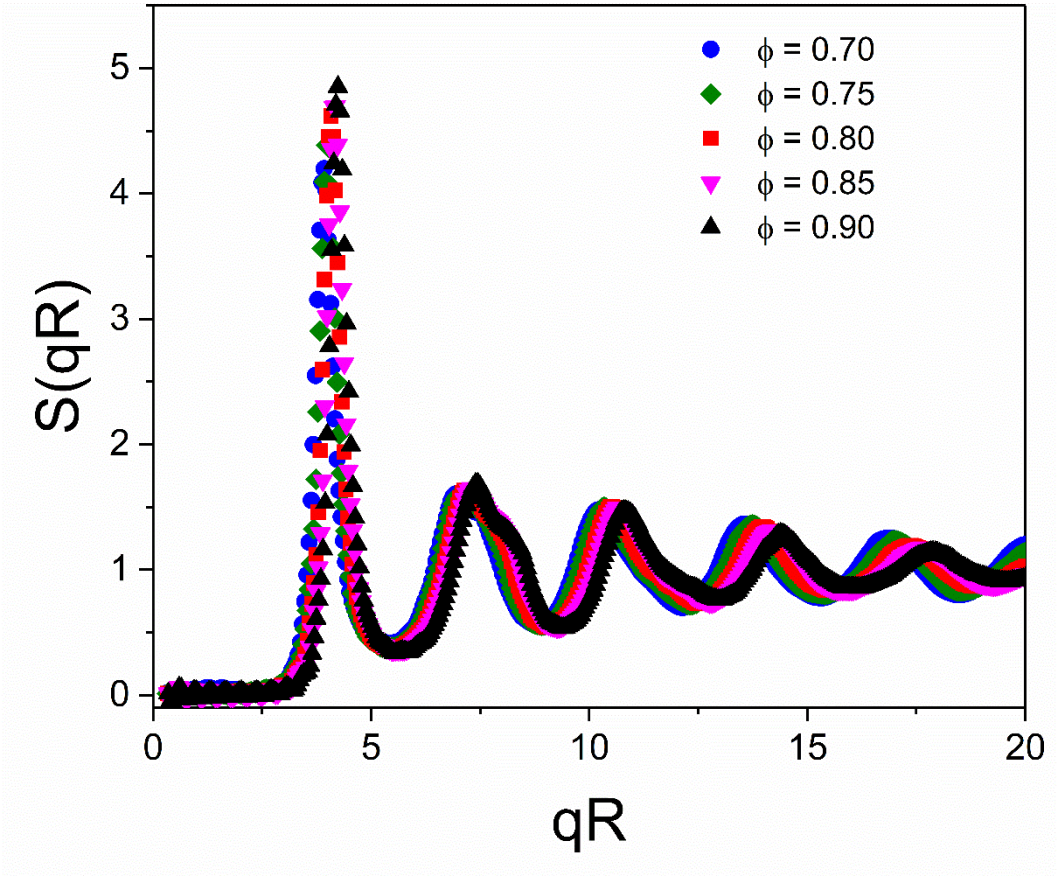

Fig. S6: Structure factor obtained at quiescent condition for suspensions with different volume fractions.

Figure S7

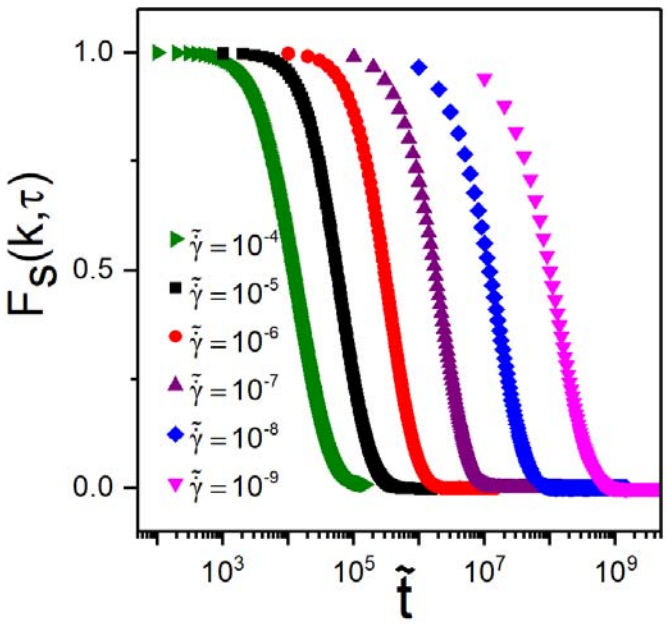

FIG S7. Intermediate scattering function as function of the normalized time $\tilde{t} = t\eta_S / E^*$ obtained at different shear rates for a SPG with a volume fraction of 0.8.

Figure S8

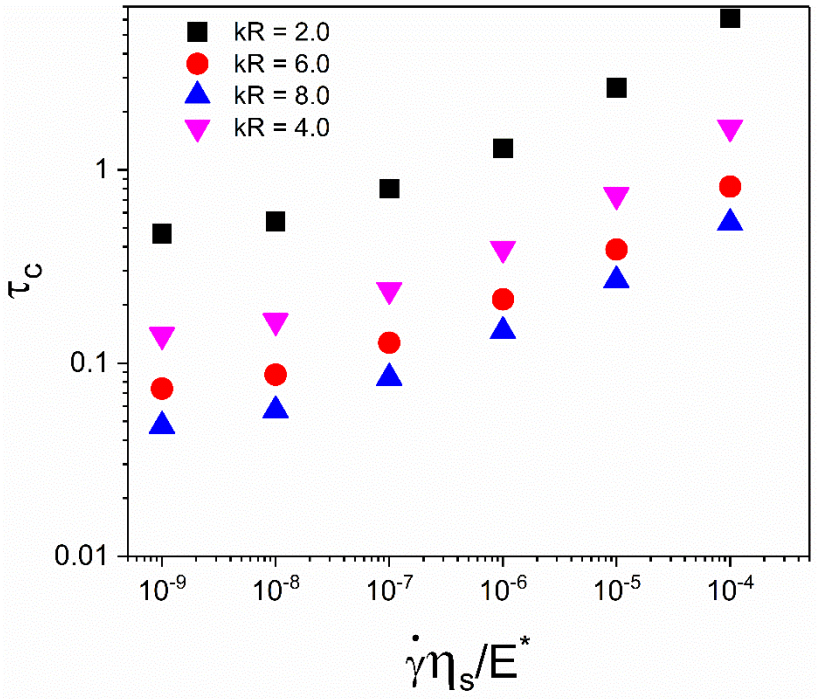

FIG S8. Values of the microscopic relaxation time (τ_C) obtained at different *kR* values for a suspension with a volume fraction of 0.8.

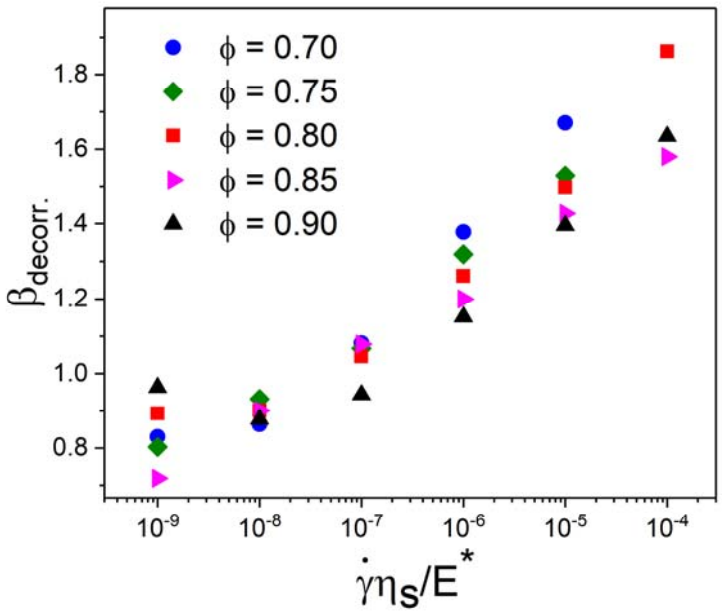

FIG S9. Values of the exponent β obtained from fitting the elastic force autocorrelation to $f(\tau) = \exp\left(-(\tau/\tau_d)^{\beta}\right)$ as a function of the shear rate for suspensions with different volume fractions.

TABLE S1: Variations of the shear stress (σ/E^*), first (N_1/E^*) and second normal ($-N_2/E^*$) stress computed at different shear rates.

$\dot{\gamma}\eta_s/E^*$	σ/E^*	N_1/E^*	$-N_2/E^*$
	$\phi = 0.70$		
10^{-5}	2.57×10^{-3}	3.61×10^{-4}	8.67×10^{-4}
10^{-6}	8.23×10^{-4}	6.53×10^{-5}	2.17×10^{-4}
10^{-7}	3.24×10^{-4}	2.09×10^{-5}	6.68×10^{-5}
10^{-8}	1.65×10^{-4}	1.22×10^{-5}	2.64×10^{-5}
10^{-9}	1.06×10^{-4}	8.89×10^{-6}	1.51×10^{-5}
	$\phi = 0.75$		
10^{-5}	4.14×10^{-3}	4.30×10^{-4}	1.28×10^{-3}
10^{-6}	1.46×10^{-3}	1.38×10^{-4}	3.45×10^{-4}
10^{-7}	6.34×10^{-4}	6.27×10^{-5}	1.19×10^{-4}
10^{-8}	3.65×10^{-4}	3.46×10^{-5}	5.55×10^{-5}
10^{-9}	2.67×10^{-4}	2.52×10^{-5}	3.50×10^{-5}
	$\phi = 0.80$		
10^{-4}	1.77×10^{-2}	4.07×10^{-3}	7.46×10^{-3}
10^{-5}	6.39×10^{-3}	5.76×10^{-4}	1.89×10^{-3}
10^{-6}	2.50×10^{-3}	2.42×10^{-4}	5.47×10^{-4}
10^{-7}	1.26×10^{-3}	1.11×10^{-4}	2.09×10^{-4}
10^{-8}	7.90×10^{-4}	7.73×10^{-5}	1.00×10^{-4}
10^{-9}	6.23×10^{-4}	6.17×10^{-5}	8.67×10^{-5}
	$\phi = 0.85$		
10^{-4}	2.91×10^{-2}	4.20×10^{-3}	9.92×10^{-3}
10^{-5}	9.94×10^{-3}	1.08×10^{-3}	2.52×10^{-3}
10^{-6}	4.11×10^{-3}	4.79×10^{-4}	7.82×10^{-4}
10^{-7}	2.24×10^{-3}	2.11×10^{-4}	3.26×10^{-4}
10^{-8}	1.55×10^{-3}	1.51×10^{-4}	1.94×10^{-4}
10^{-9}	1.31×10^{-3}	1.36×10^{-4}	1.75×10^{-4}
	$\phi = 0.90$		
10^{-4}	4.15×10^{-2}	5.43×10^{-3}	1.29×10^{-2}
10^{-5}	1.53×10^{-2}	1.41×10^{-3}	3.62×10^{-3}
10^{-6}	6.83×10^{-3}	7.30×10^{-4}	1.21×10^{-3}
10^{-7}	3.97×10^{-3}	4.00×10^{-4}	5.47×10^{-4}
10^{-8}	2.86×10^{-3}	2.57×10^{-4}	3.54×10^{-4}
10^{-9}	2.60×10^{-3}	2.35×10^{-4}	3.38×10^{-4}

TABLE S2: Crossover time (τ_m) between the ballistic and diffusive regimes, relaxation time of the elastic force (τ_d), and non-dimensional amplitude of the force fluctuations, $\hat{F}_0$, computed at different shear rates.

$\dot{\gamma}\eta_s/E^*$	τ_m	τ_d	$\hat{F}_0$
	$\phi = 0.70$		
10^{-5}	0.3549	0.2523	5.3216
10^{-6}	0.2290	0.1466	0.9877
10^{-7}	0.0951	0.0575	0.1965
10^{-8}	0.0251	0.0163	0.0444
10^{-9}	0.0080	0.0035	0.0111
	$\phi = 0.75$		
10^{-5}	0.3332	0.2201	3.0362
10^{-6}	0.1669	0.1149	0.5706
10^{-7}	0.0613	0.0388	0.1215
10^{-8}	0.0169	0.0095	0.0306
10^{-9}	0.0047	0.0016	0.0069
	$\phi = 0.80$		
10^{-4}	0.4704	0.2847	7.7072
10^{-5}	0.3209	0.1771	1.4805
10^{-6}	0.1565	0.0841	0.2880
10^{-7}	0.0677	0.0262	0.0655
10^{-8}	0.0113	0.0059	0.0177
10^{-9}	0.0025	0.0009	0.0050
	$\phi = 0.85$		
10^{-4}	0.6433	0.2666	4.5723
10^{-5}	0.3490	0.1466	0.8596
10^{-6}	0.1545	0.0615	0.1774
10^{-7}	0.0441	0.0168	0.0445
10^{-8}	0.0107	0.0039	0.0123
10^{-9}	0.0018	0.0004	0.0034
	$\phi = 0.90$		
10^{-4}	0.2710	0.2250	2.9294
10^{-5}	0.1790	0.1170	0.5879
10^{-6}	0.0443	0.0435	0.1285
10^{-7}	0.0130	0.0115	0.0321
10^{-8}	0.0030	0.0020	0.0087
10^{-9}	0.00037	0.0002	0.0032

TABLE S3: Long-time diffusion coefficient ($D\eta_s/R^2E^*$) computed at different shear rates.

$\dot{\gamma}\eta_s/E^*$	$D\eta_s/R^2E^*$
$\phi = 0.70$	
10^{-5}	6.38×10^{-7}
10^{-6}	1.26×10^{-7}
10^{-7}	2.25×10^{-8}
10^{-8}	3.72×10^{-9}
10^{-9}	5.21×10^{-10}
$\phi = 0.75$	
10^{-5}	8.08×10^{-7}
10^{-6}	1.61×10^{-7}
10^{-7}	2.94×10^{-8}
10^{-8}	4.42×10^{-9}
10^{-9}	5.71×10^{-10}
$\phi = 0.80$	
10^{-4}	4.58×10^{-6}
10^{-5}	9.91×10^{-7}
10^{-6}	1.99×10^{-7}
10^{-7}	3.41×10^{-8}
10^{-8}	5.27×10^{-9}
10^{-9}	6.09×10^{-10}
$\phi = 0.85$	
10^{-4}	5.62×10^{-6}
10^{-5}	1.21×10^{-6}
10^{-6}	2.31×10^{-7}
10^{-7}	3.96×10^{-8}
10^{-8}	5.74×10^{-9}
10^{-9}	6.00×10^{-10}
$\phi = 0.90$	
10^{-4}	7.02×10^{-6}
10^{-5}	1.44×10^{-6}
10^{-6}	2.69×10^{-7}
10^{-7}	4.36×10^{-8}
10^{-8}	5.73×10^{-9}
10^{-9}	6.05×10^{-10}

TABLE S4: Microstructural relaxation time (τ_C) computed at different shear rates.

$\dot{\gamma}\eta_s / E^*$	τ_C
$\phi = 0.70$	
10^{-5}	1.09209
10^{-6}	0.55138
10^{-7}	0.31524
10^{-8}	0.20551
10^{-9}	0.15855
$\phi = 0.75$	
10^{-5}	0.84224
10^{-6}	0.43394
10^{-7}	0.25666
10^{-8}	0.17703
10^{-9}	0.14685
$\phi = 0.80$	
10^{-4}	1.70187
10^{-5}	0.68995
10^{-6}	0.3606
10^{-7}	0.22017
10^{-8}	0.16076
10^{-9}	0.13934
$\phi = 0.85$	
10^{-4}	1.32167
10^{-5}	0.56946
10^{-6}	0.31083
10^{-7}	0.19723
10^{-8}	0.1533
10^{-9}	0.1402
$\phi = 0.90$	
10^{-4}	0.98994
10^{-5}	0.47455
10^{-6}	0.27303
10^{-7}	0.18481
10^{-8}	0.15105
10^{-9}	0.14307